
























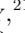











A New Brown Dwarf Orbiting an M star and An Investigation on the Eccentricity Distribution of Transiting Long-Period Brown Dwarfs

TIANJUN GAN ¹ CHARLES CADIEUX ² SHIGERU IDA ³ SHARON X. WANG ⁴ SHUDE MAO ¹ ZITAO LIN ⁴
KEIVAN G. STASSUN ^{5,6} ADAM J. BURGASSER ⁷ STEVE B. HOWELL ⁸ CATHERINE A. CLARK ⁹
IVAN A. STRAKHOV ¹⁰ PAUL BENNI ¹¹ GEORGE R. RICKER ¹² ROLAND VANDERSPEK ¹² DAVID W. LATHAM ¹³
SARA SEAGER ^{12,14,15} JOSHUA N. WINN ¹⁶ JON M. JENKINS ⁸ LUC ARNOLD ¹⁷ ÉTIENNE ARTIGAU ^{2,18}
DAVID CHARBONNEAU ¹³ KAREN A. COLLINS ¹³ NEIL J. COOK ² ZOË L. DE BEURS ^{14,19} SARAH J. DEVENY ^{20,8}
JOHN P. DOTY ²¹ RENÉ DOYON ^{2,18} COLIN LITTLEFIELD ^{20,8} TYLER PRITCHARD ²² GABRIELLE ROSS ¹⁶
AVI SHPORER ¹² CHRISTOPHER R. THEISSEN ⁷ BENJAMIN M. TOFFLEMIRE ²³ ANDREW VANDERBURG ^{12,24} AND
DAVID WATANABE ²⁵

¹Department of Astronomy, Westlake University, Hangzhou 310030, Zhejiang Province, China

²Université de Montréal, Département de Physique, IREX, Montréal, QC H3C 3J7, Canada

³Earth-Life Science Institute, Institute of Science Tokyo, Meguro, Tokyo 152-8550, Japan

⁴Department of Astronomy, Tsinghua University, Beijing 100084, China

⁵Department of Physics and Astronomy, Vanderbilt University, 6301 Stevenson Center Ln., Nashville, TN 37235, USA

⁶Department of Physics, Fisk University, 1000 17th Avenue North, Nashville, TN 37208, USA

⁷Department of Astronomy & Astrophysics, University of California, San Diego, 9500 Gilman Dr, La Jolla, CA 92093, USA

⁸NASA Ames Research Center, Moffett Field, CA 94035, USA

⁹NASA Exoplanet Science Institute-Caltech/IPAC, Pasadena, CA 91125, USA

¹⁰Sternberg Astronomical Institute, Lomonosov Moscow State University, 119992 Universitetskii prospekt 13, Moscow, Russia

¹¹Acton Sky Portal (private observatory), Acton, MA USA

¹²Department of Physics and Kavli Institute for Astrophysics and Space Research, Massachusetts Institute of Technology, Cambridge, MA 02139, USA

¹³Center for Astrophysics | Harvard & Smithsonian, 60 Garden Street, Cambridge, MA 02138, USA

¹⁴Department of Earth, Atmospheric and Planetary Science, Massachusetts Institute of Technology, 77 Massachusetts Avenue, Cambridge, MA 02139, USA

¹⁵Department of Aeronautics and Astronautics, MIT, 77 Massachusetts Avenue, Cambridge, MA 02139, USA

¹⁶Department of Astrophysical Sciences, Princeton University, 4 Ivy Lane, Princeton, NJ 08544, USA

¹⁷Canada–France–Hawaii Telescope, 65-1238 Mamalahoa Hwy, Kamuela, HI 96743, USA

¹⁸Observatoire du Mont-Mégantic, Université de Montréal, Montréal, QC H3C 3J7, Canada

¹⁹NSF Graduate Research Fellow, MIT Presidential Fellow, MIT Collamore-Rogers Fellow, MIT Teaching Development Fellow

²⁰Bay Area Environmental Research Institute, Moffett Field, CA 94035, USA

²¹Noqi Aerospace Ltd., 15 Blanchard Avenue, Billerica, MA 01821, USA

²²NASA Goddard Space Flight Center, 8800 Greenbelt Road, Greenbelt, MD 20771, USA

²³SETI Institute, Mountain View, CA 94043 USA/NASA Ames Research Center, Moffett Field, CA 94035 USA

²⁴Sloan Fellow

²⁵Planetary Discoveries, Valencia, CA 91354, USA

ABSTRACT

The orbital eccentricities of brown dwarfs encode valuable information of their formation and evolution history, providing insights into whether they resemble giant planets or stellar binaries. Here, we report the discovery of TOI-5575b, a long-period, massive brown dwarf orbiting a low-mass M5V star ($0.21 \pm 0.02 M_{\odot}$) delivered by the TESS mission. The companion has a mass and radius of $72.4 \pm 4.1 M_J$ and $0.84 \pm 0.07 R_J$ on a 32-day moderately eccentric orbit ($e = 0.187 \pm 0.002$), making it the third highest-mass-ratio transiting brown dwarf system known to date. Building on this discovery, we investigate the eccentricity distributions of a sample of transiting long-period ($10 \leq P \lesssim 1000$ days,

Corresponding author: Tianjun Gan

tianjungan@gmail.com

$\sim 0.1\text{--}1.5$ AU) giant planets, brown dwarfs and low-mass stars. We find that brown dwarfs exhibit an eccentricity behavior nearly identical to that of giant planets: a preference for circular orbits with a long tail toward high eccentricities. Such a trend contrasts sharply with direct imaging findings, where cold (5–100 AU) brown dwarfs and giant planets display distinct eccentricity distributions. Our results suggest that transiting long-period brown dwarfs and giant planets probably 1) form in different routes at exterior orbits but undergo analogous dynamical evolution processes and migrate inwards; or 2) both contain two sub-groups, one with widely spread eccentricities while the other has circular orbits, that jointly sculpt the eccentricity distributions. The low-mass-star systems appear to be a distinctive population, showing a peak eccentricity at about 0.3, akin to more massive stellar binaries.

Keywords: Brown dwarfs; Transit photometry; Radial velocity; Eccentricity; Stars: individual (TIC 160162137, TOI-5575)

1. INTRODUCTION

As intermediate objects between giant planets and low-mass stars, brown dwarfs (BDs) have masses above the deuterium burning limit ($\sim 13 M_J$, Burgasser et al. 2003; Spiegel et al. 2011) and below the threshold of hydrogen fusion ($\sim 80 M_J$, Laughlin et al. 1997). Early blind radial velocity (RV) surveys have identified that brown dwarfs around Sun-like stars within 3 AU are much rarer compared to planets and stellar companions, manifesting as a “brown dwarf desert” (Marcy & Butler 2000). Such an occurrence rate deficit suggests that brown dwarfs are probably more challenging to form compared with the other two categories or that subsequent dynamical processes are unlikely to push brown dwarfs inwards after formation (Grether & Lineweaver 2006). Nevertheless, the number of transiting brown dwarfs has been enlarging dramatically during the past decade (e.g., Artigau et al. 2021; Psaridi et al. 2022; Carmichael et al. 2022; Lin et al. 2023; Henderson et al. 2024; Larsen et al. 2025). It remains under debate how such massive objects, in particular those having orbital periods $P \geq 10$ days, ended up at their current locations.

Regarding the origins of warm Jupiters, three hypotheses have been postulated including in-situ formation, disk-driven migration, and high-eccentricity migration (Dawson & Johnson 2018). One route to probe the predominant scenario of the evolution channel is investigating the orbital eccentricities (e.g., Dawson & Johnson 2012; Dong et al. 2021), on which different mechanisms have different predictions. After initially forming through either core accretion (Pollack et al. 1996) or gravitational instability (Boss 2000), giant planets are expected to undergo dynamical interactions with other bodies or the disk (Dawson & Johnson 2018), and migrate inwards (Lin et al. 1996). During their evolution, giant planets could gather angular momentum and develop orbital eccentricities through, for exam-

ple, planet-planet scattering (Rasio & Ford 1996; Dawson & Murray-Clay 2013; Petrovich & Tremaine 2016), planet-disk interactions (Goldreich & Sari 2003) and Kozai–Lidov perturbations with outer massive companions (Naoz et al. 2011). Recent work from Alqasim et al. (2025) looked into transiting long-period giant planet systems with $P > 10$ days, and identified a positive correlation between eccentricity and stellar metallicity (see also Dawson & Murray-Clay 2013) but found no correlation between eccentricity and the presence of a second stellar companion (see also Stevenson et al. 2025), suggesting that planet-planet scattering (Naoz et al. 2011; Beaugé & Nesvorný 2012; Carrera et al. 2019) is more likely to be the way that produce warm Jupiters instead of the Kozai–Lidov effect (Fabrycky & Tremaine 2007). On the other hand, stellar binaries are supposed to form through protostellar core or disk fragmentation (Kratter & Lodato 2016) instead and migrate inwards driven by Kozai–Lidov interactions (Eggleton & Kisseleva-Eggleton 2006; Naoz & Fabrycky 2014) or accreting from the circumbinary disc (Tokovinin & Moe 2020). All these formation and dynamical processes are expected to conjunctly shape the final eccentricity distribution of the companion.

However, brown dwarfs remain poorly understood on their evolution due to the limited number of detections that impede statistical studies, leaving a fundamental question unresolved: do brown dwarfs follow the routes of giant planets or more approximate to stellar binaries? Early work from Ma & Ge (2014) reported that brown dwarfs with masses above and below $42.5 M_J$ exhibit different eccentricity distributions: the massive population behaves like stellar binaries while the less massive group is more alike to planets, implying two different formation channels. Ma & Ge (2014) made use of brown dwarfs mostly detected by radial velocity surveys and thus only have minimum masses available. According to recent results from Gaia astrometry, it turns out

that several previously RV-detected brown dwarfs probably require reclassification as they are no longer located in the sub-stellar mass regime with true masses above $80 M_J$ (Unger et al. 2023). More recently, Vowell et al. (2025) questioned the existence of the mass transition point by looking into the mass ratio and metallicity distributions of brown dwarfs. Moving outwards, Bowler et al. (2020) found that directly-imaged brown dwarfs and giant planets between 5 and 100 AU have significantly different eccentricity preferences (see also Nagpal et al. 2023; Do Ó et al. 2023). Cold Jupiters tend to exhibit small eccentricities peaking at around 0.05-0.25 while wide-orbit brown dwarfs have a broad eccentricity distribution, favoring higher values ($e \sim 0.6$ -0.9). It is yet unclear if inner Jupiter-like planets and brown dwarfs follow the same trend. The increasing number of transiting brown dwarfs now enables a glimpse into their orbital eccentricity distribution and compare that with other two companion classes, which could in turn offer insights into their origins.

In this paper, we first report the discovery of TOI-5575 b, a long-period massive brown dwarf around a low-mass star. Afterwards, we carry out population-level comparative studies between transiting long-period gas giants, brown dwarfs and low-mass stars. The paper is organized as follows. In Section 2, we describe all observations we collected to confirm TOI-5575 b. We perform the stellar characterization and a joint analysis of photometric and RV data in Section 3. Section 4 details how we select the samples, and conduct the eccentricity distribution comparison. We discuss our results in Section 5 and conclude our findings in Section 6.

2. OBSERVATIONS

2.1. TESS and Ground-Based Photometry

TOI-5575 (TIC 160162137) was first observed by the Transiting Exoplanets Survey Satellite (TESS; Ricker et al. 2015) in six Sectors every 30 minutes between 2019 and 2020. Subsequent monitoring during the First Extended Mission covered five additional sectors at a 10-minute cadence, followed by five more sectors at a 2-minute cadence during the ongoing Second Extended Mission. Due to the faintness of the host star ($T_{\text{mag}} = 14.0$), we note that the photometry of TOI-5575 during the TESS Primary Mission is not available since the Quick Look Pipeline (QLP; Huang et al. 2020a,b) produce light curves of objects down to $T_{\text{mag}} = 13.5$ and only those down to $T_{\text{mag}} = 10.5$ are searched for transits. The candidate was not alerted until the initiation of the QLP faint-star search program (Kunimoto et al. 2022).

Table 1. Summary of stellar properties for TOI-5575.

Parameter	Value	Ref.
<i>Main identifiers</i>		
TIC	160162137	TIC V8.2 ^[1]
<i>Gaia</i> ID	1724291831608394624	<i>Gaia</i> DR3 ^[2]
<i>Equatorial Coordinates</i>		
$\alpha_{J2015.5}$	16:04:59.65	TIC V8.2
$\delta_{J2015.5}$	+85:12:17.01	TIC V8.2
<i>Photometric properties</i>		
<i>TESS</i> (mag)	14.013 ± 0.007	TIC V8.2
<i>V</i> (mag)	17.010 ± 0.200	TIC V8.2
<i>G</i> (mag)	15.352 ± 0.001	<i>Gaia</i> DR3
<i>G_{BP}</i> (mag)	17.102 ± 0.004	<i>Gaia</i> DR3
<i>G_{RP}</i> (mag)	14.093 ± 0.001	<i>Gaia</i> DR3
<i>J</i> (mag)	12.281 ± 0.021	2MASS ^[3]
<i>H</i> (mag)	11.723 ± 0.017	2MASS
<i>K</i> (mag)	11.436 ± 0.019	2MASS
<i>W1</i> (mag)	11.266 ± 0.023	WISE ^[4]
<i>W2</i> (mag)	11.061 ± 0.020	WISE
<i>W3</i> (mag)	10.815 ± 0.060	WISE
<i>Astrometric properties</i>		
ϖ (mas)	17.784 ± 0.027	<i>Gaia</i> DR3
μ_{α} (mas yr ⁻¹)	-19.181 ± 0.032	<i>Gaia</i> DR3
μ_{δ} (mas yr ⁻¹)	131.205 ± 0.034	<i>Gaia</i> DR3
RV (km s ⁻¹)	-38.8 ± 4.2	<i>Gaia</i> DR3
<i>Stellar parameters</i>		
Spectral Type	$M5.0 \pm 0.5$	This work
Distance (pc)	56.2 ± 0.1	This work
M_* (M_{\odot})	0.21 ± 0.02	This work
R_* (R_{\odot})	0.24 ± 0.02	This work
$\log g_*$ (cgs)	5.00 ± 0.04	This work
T_{eff} (K)	3115 ± 100	This work
[Fe/H] (dex)	-0.21 ± 0.07	This work

[1]Stassun et al. (2019); [2]Gaia Collaboration et al. (2023); [3]Cutri et al. (2003); [4]Wright et al. (2010).

To homogeneously extract the light curves from the TESS Primary Mission, we performed uniform aperture photometry using the `lightkurve` package (Lightkurve Collaboration et al. 2018), following the procedures in Gan et al. (2023). In short, we first obtain the photometry using a custom 3×3 box aperture centering at the target star, and then subtract it with the time-series of the background. The light curves from the TESS First and Second Extended Missions were extracted using the QLP and by the Science Processing Operations Center (SPOC; Jenkins et al. 2016; Stumpe et al. 2012, 2014; Smith et al. 2012), respectively. For the SPOC data, we use the simple aperture photometry without light dilution correction. We then employ the `celerite` algorithm (Foreman-Mackey et al. 2017) to detrend the light curve by fitting a Gaussian Process (GP) model with a Matérn-3/2 kernel to the out-of-transit data. The detrending was carried out independently for TESS data obtained during three Missions since the observational cadences and the sources of photometry are different. Figure A1 presents the raw and detrended TESS light curves.

In addition to the TESS data, we collected a ground-based light curve using the 0.36-m Acton-Sky-Portal (ASP) telescope on 2023 December 14. The observation was conducted in a blue-blocking clear (CBB) filter and fully covered the transit event. The ASP telescope is equipped with an SBIG Aluma CCD47-10 camera with a plate scale of 1 arcsec per pixel, providing a $17' \times 17'$ field of view. We performed the photometric analysis using the *AstroImageJ* package (Collins et al. 2017) with an uncontaminated $5''$ aperture.

2.2. Spectroscopic Follow-up Observations

2.2.1. CFHT/SPIRou Radial Velocities

We obtained a total of 27 SPIRou (SpectroPolarimètre InfraROUge; Donati et al. 2020) spectra of TOI-5575 between UT 2023 May 1 and UT 2023 June 30 to determine the mass of the transiting companion. SPIRou is a near-infrared spectropolarimeter installed on the 3.6-m Canada-France-Hawaii Telescope (CFHT), offering a spectral resolution of $R \approx 75,000$ and covering the $0.95\text{--}2.35\text{ }\mu\text{m}$ wavelength range. The observations were carried out over thirteen nights usually with two consecutive 1200s exposures per night under an environment condition of airmass around 2.4 and seeing about $0.6''$. The median signal-to-noise ratio (SNR) of our spectra is 16 per pixel in the center of the H band ($\sim 1.7\text{ }\mu\text{m}$).

The raw SPIRou data were reduced with the *APERIO* pipeline (Cook et al. 2022), which produced telluric-corrected spectra. We then measured the radial velocities from these telluric-corrected spectra through the line-by-line (LBL) method of Artigau et al. (2022), employing a high SNR template of Gliese 699 (M4V) observed with SPIRou instead of TOI-5575 to improve the precision. We discarded three epochs with outlying RV due to a low SNR below 5, leaving a final set of 24 measurements taken over 12 independent nights (see Figure 1). We measure a systemic velocity of about -45.9 km s^{-1} for TOI-5575, which agrees with the result of $-38.8 \pm 4.2\text{ km s}^{-1}$ from Gaia (Gaia Collaboration et al. 2023). Table B1 lists the final SPIRou RV measurements that reached a median precision of 18.5 m s^{-1} .

2.2.2. Keck/NIRES

TOI-5575 was observed with the Near-Infrared Echellette Spectrometer (NIREs; Wilson et al. 2004) mounted on the Keck II 10m telescope on UT 2025 May 16 in clear conditions with $1''$ seeing. NIREs provides $1.0\text{--}2.4\text{ }\mu\text{m}$ spectroscopy in four cross-dispersed orders at an average resolution of $\lambda/\Delta\lambda \approx 2700$ for its fixed $0''.55$ -wide slit (Figure C1). The source was observed over two series of ABBA sequences (8 exposures) nodding along the $10''$ slit, with 120 s exposures. Data were reduced

using a modified version of Spextool (Cushing et al. 2004) following standard extraction procedures and the flux/telluric correction algorithm of Vacca et al. (2003).

2.3. High Angular Resolution Imaging

We performed high-resolution speckle imaging observations to search for close-in unresolved stellar companions.

We observed TOI-5575 on UT 2023 May 6 with the speckle polarimeter on the 2.5-m telescope at the Caucasian Observatory of Sternberg Astronomical Institute (SAI) of Lomonosov Moscow State University. A low-noise CMOS detector Hamamatsu ORCA-quest (Strakhov et al. 2023) was used as a detector. The atmospheric dispersion compensator was active, which allowed using the I_c band. The respective angular resolution is $0.083''$. No companion was detected. The detection limits at distances 0.25 and $1.0''$ from the star are $\Delta I_c = 2.2$ and 4.5 magnitudes, see Figure D1.

TOI-5575 was also observed on UT 2025 April 14 using the ‘Alopeke speckle instrument on the Gemini North 8-m telescope (Scott et al. 2021). ‘Alopeke provides simultaneous speckle imaging in two filters with output data products including reconstructed images and robust contrast limits on companion detections (Howell et al. 2016). Ten sets of 1000×0.06 sec exposures were collected for TOI-5575 at 562 nm, 832 nm, SDSS r , and SDSS z , and were reduced following the standard reduction pipeline (Howell et al. 2011). Figure D1 shows the final 5σ magnitude contrast curves and the 832 nm and SDSS z -band reconstructed images. There are hints of a close-in companion in the reconstructed z -band image, the signal of which is likely caused by imaging smearing and significant chromatic effects due to the high airmass (Clark et al. 2024). Furthermore, TOI-5575 has a RUWE value of 1.2, which is consistent with a single star (Ziegler et al. 2020; Gaia Collaboration et al. 2021). We also find no RV linear trend in our SPIRou data (see Section 3.2). While we cannot rule out the presence of a close-in ($< 1''$) companion entirely, we find it unlikely to be real for the reasons above. No other companion brighter than 4-5 magnitudes was detected down to the diffraction limit of the telescope (20 mas) out to $1.2''$ (1.1 to 68 au).

3. ANALYSIS

3.1. Stellar Characterization

Figure C1 displays the reduced NIREs spectrum of TOI-5575 with telluric absorption regions masked, compared to similar data of the best-matching M5 standard Gliese 866AB from Cushing et al. (2005). We use the relations of Mann et al. (2014) to infer $[\text{Fe}/\text{H}] =$

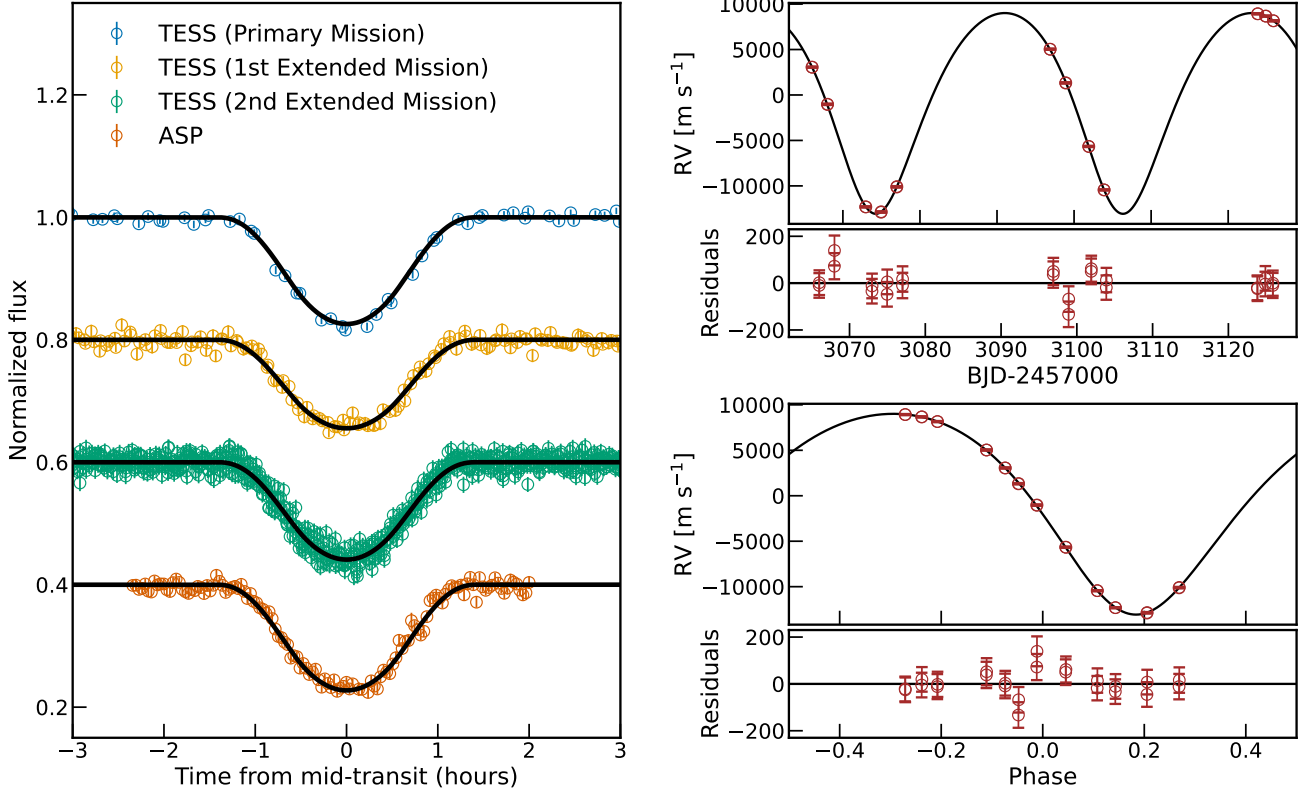


Figure 1. *Left panel:* The TESS and ASP light curves folded in phase with the transit ephemeris from the joint analysis along with the best-fit transit models. *Right panel:* The full SPIRou RV timeseries and the phase-folded RVs. The error bars presenting here are the quadrature sum of the original RV uncertainties and the instrument jitter. The black solid line is the best-fit Keplerian model. The residuals are shown below each subplot.

-0.21 ± 0.07 based on a combination of H_2O -K2 color and $2.20 \mu\text{m}$ Na I and $2.26 \mu\text{m}$ Ca I equivalent widths. We infer equivalent subsolar metallicities based on near-infrared relations defined in Rojas-Ayala et al. (2012); Terrien et al. (2012); and Newton et al. (2014).

We next estimate the stellar properties based on empirical relations. We compute the absolute magnitude $M_K = 7.69 \pm 0.02$ of TOI-5575 based on the m_K from 2MASS and parallax from *Gaia* DR3. By utilizing the polynomial relation between R_* and M_K derived in Mann et al. (2015), we obtain a stellar radius of $0.24 \pm 0.02 R_\odot$. In addition, we find a stellar mass of $0.21 \pm 0.02 M_\odot$ according to the M_* - M_K relation (Mann et al. 2019), which agrees well with the result of $0.21 \pm 0.02 M_\odot$ from Benedict et al. (2016). Finally, the stellar effective temperature T_{eff} is estimated to be $3115 \pm 100 \text{ K}$ through a polynomial relation with stellar colors $V-J$ and $J-H$ (Mann et al. 2015), in accord with $3029 \pm 120 \text{ K}$ from (Pecaut & Mamajek 2013), which is also based on an empirical equation but between T_{eff} and $V-K$.

We also independently determine the stellar radius and effective temperature of TOI-5575 by carrying out

a spectral energy distribution (SED) analysis (Stassun & Torres 2016; Stassun et al. 2017; Stassun & Torres 2018). We pull the JHK magnitudes from 2MASS (Cutri et al. 2003), the $W1$, $W2$ and $W3$ magnitudes from WISE (Wright et al. 2010) as well as three *Gaia* magnitudes G , G_{BP} , G_{RP} from *Gaia* DR3 (Gaia Collaboration et al. 2023), all listed in Table 1. Together, the available photometry spans the wavelength range 0.5–10 μm (Figure C1). We perform a fit using PHOENIX stellar atmosphere models (Husser et al. 2013), with the free parameters being the effective temperature (T_{eff}) and metallicity ($[\text{Fe}/\text{H}]$). Given the proximity of the host star, we fix the extinction A_V to 0. The best-fit has a reduced χ^2 of 1.8 with $T_{\text{eff}} = 3175 \pm 100 \text{ K}$ and $[\text{Fe}/\text{H}] = -0.3 \pm 0.5 \text{ dex}$, consistent with the result we obtained from the NIRES spectrum. The metallicity is further constrained by the *Gaia* spectrum (see gray swathe in the inset of Figure C1). Integrating the (unreddened) model SED gives the bolometric flux at Earth, $F_{\text{bol}} = 5.32 \pm 0.19 \times 10^{-11} \text{ erg s}^{-1} \text{ cm}^{-2}$. Taking the F_{bol} and T_{eff} together with the *Gaia* DR3 parallax leads to the stellar radius $R_* = 0.24 \pm 0.02 R_\odot$, consistent

with the estimation above. The final stellar parameters adopted for further analysis are listed in Table 1.

3.2. Joint Fit of Transit and RV data

We utilize the *juliet* (Espinoza et al. 2019) package to perform a joint fit to the space and ground-based photometry together with the SPIRou radial velocity data in order to determine the physical parameters of the companion. To summarize, *juliet* makes use of *batman* (Kreidberg 2015) to fit the light curves and *radvel* (Fulton et al. 2018) to build the standard RV model. We apply the dynamic nested sampling method with *dynesty* (Speagle 2020) to obtain the posteriors of each parameter.

Since the TESS images taken during the Primary, First Extended and Second Extended Missions have different cadences, we treat the data as if they were from three different instruments in the joint fit. Due to the relatively large pixel scale ($21'' \times 21''$) of TESS, we fit dilution factors¹ for the TESS photometry to account for the potential light contamination from other stars. We fix it at 1 for the ground-based ASP data because of its small pixel scale that deblends all nearby stars. We adopt the quadratic limb darkening law (q_1 and q_2 ; Kipping 2013) for both TESS and ASP data. Moreover, we also model the relative out-of-transit target flux for each photometric dataset and incorporate a jitter term to take additional white noises into account.

Regarding the RV modeling, the short time span and the limited number of our SPIRou observations make it insufficient to search for Keplerian signals from additional outer planets other than the one from TOI-5575b, hence we focus exclusively on the Keplerian model of a single companion and fix the linear and quadratic RV trends at zero². As the companion has a long orbital period and tidal effects are weak (see Section 3.3), we fit an eccentric orbit, leaving $e \sin \omega$ and $e \cos \omega$ as free parameters. We also model a constant RV offset and consider possible additional systematics by fitting an RV jitter, which is added in quadrature to the original RV uncertainties. We allow all parameters to vary uniformly or loguniformly except for the orbital period and mid-transit time, on which we place narrow Gaussian normal priors, centering at the results from transit search with 1σ values of 0.1 days. All photometric and RV data along with the best-fit transit and Keplerian models are

illustrated in Figure 1. The priors we set and the resulting best-fit key parameters are summarized in Table 2.

We next perform a secondary eclipse analysis by masking out the secondary eclipse data based on the joint fit and then detrending the light curve with GP. We do not find any secondary eclipse signal in the TESS light curve with depth larger than 1.3% (3σ confidence level). Supposing that the companion is a very-low-mass M dwarf with $M_* = 0.08 M_\odot$, the expected secondary eclipse depth in the TESS spectral bandpass would be about 2.3%, assuming blackbody spectra without reflected starlight (Charbonneau et al. 2005). Consequently, we conclude that the companion is a massive brown dwarf rather than a star at the bottom of the main sequence. We further carry out a transit timing variation (TTV) analysis by modeling the mid-transit time of individual transits of TESS and ASP data, and fit a linear ephemeris to the transit times using *juliet*. The results show that all timing variations are within 4 minutes with no significant TTV signal detected in the dataset.

3.3. TOI-5575b: A Massive Eccentric Brown Dwarf Around a Low-Mass M Star

The joint photometric and RV analysis reveals that the companion is a brown dwarf with a radius of $0.84 \pm 0.07 R_J$ and a mass of $72.4 \pm 4.1 M_J$ on a 32-day eccentric ($e = 0.187 \pm 0.002$) orbit. The location of TOI-5575b in the Mass-Radius diagram (Figure 2) aligns with the evolution track of a brown dwarf with an age of about 5-10 Gyr (Baraffe et al. 2003), suggesting that the host star is not young, which agrees with the non-detection of significant rotation signal in the light curve from Zwicky Transient Facility (ZTF; Bellm et al. 2019; Masci et al. 2019)³. Following Equation 1 in Jackson et al. (2008), we estimate the tidal circularization timescale τ_{circ} of TOI-5575b. By adopting the typical modified quality factor of the brown dwarf (Q_{BD}) and the host star (Q_*) both as 10^6 , we obtain a τ_{circ} of about 5×10^{13} years, much longer than any astrophysical timescale. Therefore, we conclude that TOI-5575b holds the primordial configuration memory of the eccentricity without being erased by tidal effects. With a period of about 32 days, TOI-5575b joins the small group of long-period substellar objects with $P > 10$ days (see the right panel of Figure 2).

TOI-5575b is so far the third highest mass ratio transiting brown dwarf system ($q = 0.329 \pm 0.037$) following ZTF J2020+5033b (El-Badry et al. 2023) and TOI-

¹ The dilution factor defined in the *juliet* package is given by $1/(1+A_D)$, where A_D is the flux ratio between contaminating sources and the target.

² An independent fit including a linear RV trend leads to a best-fit of $\dot{\gamma} = 1.1 \pm 4.4 \text{ m s}^{-1} \text{ day}^{-1}$, consistent with 0 within 1σ .

³ A total of two ZTF light curves in g and r bands are available and each has 475 data points, spanning about 5.5 years.

Table 2. Priors and the best-fit values along with the 68% credibility intervals in the final joint fit for TOI-5575. $\mathcal{N}(\mu, \sigma^2)$ is a normal prior with mean μ and standard deviation σ . $\mathcal{U}(a, b)$ represents a uniform prior between a and b . $\mathcal{LU}(a, b)$ stands for a log-uniform prior between a and b .

Parameter	Prior	Value	Description
<i>Orbit parameters</i>			
P (days)	$\mathcal{N}(32.1, 0.1)$	32.072306 ± 0.000007	Orbital period.
T_c (BJD-2457000)	$\mathcal{N}(1689.2, 0.1)$	1689.2666 ± 0.0003	Mid-transit time.
r_1	$\mathcal{U}(0, 1)$	0.6391 ± 0.0015	Parametrization for p and b ^[1] .
r_2	$\mathcal{U}(0, 1)$	0.3518 ± 0.0065	Parametrization for p and b .
$e \sin \omega$	$\mathcal{U}(-1, 1)$	0.0338 ± 0.0030	Parametrization for e and ω .
$e \cos \omega$	$\mathcal{U}(-1, 1)$	-0.1838 ± 0.0020	Parametrization for e and ω .
K (m s ⁻¹)	$\mathcal{U}(5000, 15000)$	11041.6 ± 23.5	RV semi-amplitude.
μ_{SPIRou} (m s ⁻¹)	$\mathcal{U}(-50000, -30000)$	$-45931.7 \pm 32..2$	RV offset.
σ_{SPIRou} (m s ⁻¹)	$\mathcal{U}(0, 100)$	49.8 ± 9.2	RV jitter.
<i>Stellar parameter</i>			
ρ_* (kg m ⁻³)	$\mathcal{LU}(10^2, 10^5)$	21500 ± 121	Stellar density of the host star.
<i>Dilution factors</i>			
$D_{\text{TESS,PM}}^{[2]}$	$\mathcal{U}(0, 1)$	0.997 ± 0.002	
$D_{\text{TESS,EM1}}$	$\mathcal{U}(0, 1)$	0.838 ± 0.014	
$D_{\text{TESS,EM2}}$	$\mathcal{U}(0, 1)$	0.905 ± 0.011	
D_{ASP}	1 (Fixed)	...	
<i>Derived parameters</i>			
R_c/R_*	...	0.3518 ± 0.0065	Scaled companion radius.
a/R_*	...	105.35 ± 0.21	Scaled semi-major axis.
b	...	0.459 ± 0.022	Impact parameter.
i (degrees)	...	89.73 ± 0.02	Orbital inclination.
e	...	0.187 ± 0.002	Orbital eccentricity.
ω (degrees)	...	169.6 ± 1.1	Argument of periapsis.
<i>Physical parameters of the BD</i>			
R_c (R _J)	...	0.84 ± 0.07	Companion radius.
M_c (M _J)	...	72.4 ± 4.1	Companion mass.
a (AU)	...	0.118 ± 0.010	Semi-major axis.
q	...	0.329 ± 0.037	Mass ratio between the BD and the host star.

[1] The parameters of p and b are the companion-to-star radius ratio and the impact parameter (Espinoza 2018). [2] The subscripts PM, EM1 and EM2 represent Primary Mission, First Extended Mission and Second Extended Mission. The light dilution factors are different because of the different sources of TESS photometry based on different apertures.

6508b (Barkaoui et al. 2025). Its moderate eccentricity places it among the rare sample of eccentric-orbit brown dwarfs. Figure 3 presents the eccentricity-mass diagram of known transiting brown dwarfs and low-mass stars with companion masses $M_c \leq 150 M_J$. Two key features can be seen: 1) the majority of eccentric ($e > 0.3$) companions occupy the mass range between $42.5 M_J$ and $110 M_J$; 2) most of them have orbital periods longer than 10 days. The outer mass threshold of $110 M_J$ is simply from visual inspection while the inner mass limit of $42.5 M_J$ was initially reported by Ma & Ge (2014), who found that brown dwarfs with masses above and below $42.5 M_J$ have different eccentricity distributions, indicating two different formation mechanisms. We compute the number ratios of high-eccentricity objects with $e > 0.3$ within three mass ranges: $M_c < 42.5 M_J$, $42.5 \leq M_c < 110 M_J$ and $M_c \geq 110 M_J$. We find that the fractions are 14.3%, 24.6% and 8.3%, showing a tentative increase of high-eccentricity objects with $42.5 \leq M_c < 110 M_J$. However, Vowell et al. (2025)

argued against a transition point in the eccentricity distribution when considering the systems' mass ratio (see the right panel of Figure 3), a more fundamental parameter of the formation process, where the eccentricity dichotomy seems to disappear.

4. ECCENTRICITY DISTRIBUTION

In this section, we compare the eccentricity distribution of transiting long-period giant planets, brown dwarfs as well as low-mass stars. We first outline how we build the samples in Section 4.1 and then describe the way we model the eccentricity distributions before summarizing the results in Section 4.2.

4.1. Sample Selection

We construct our brown dwarf and low-mass star samples based on a combination of two catalogs published in Vowell et al. (2025) and Barkaoui et al. (2025), supplemented with several recent detections (Larsen et al. 2025; Zhang et al. 2025) as well as the newly discovered

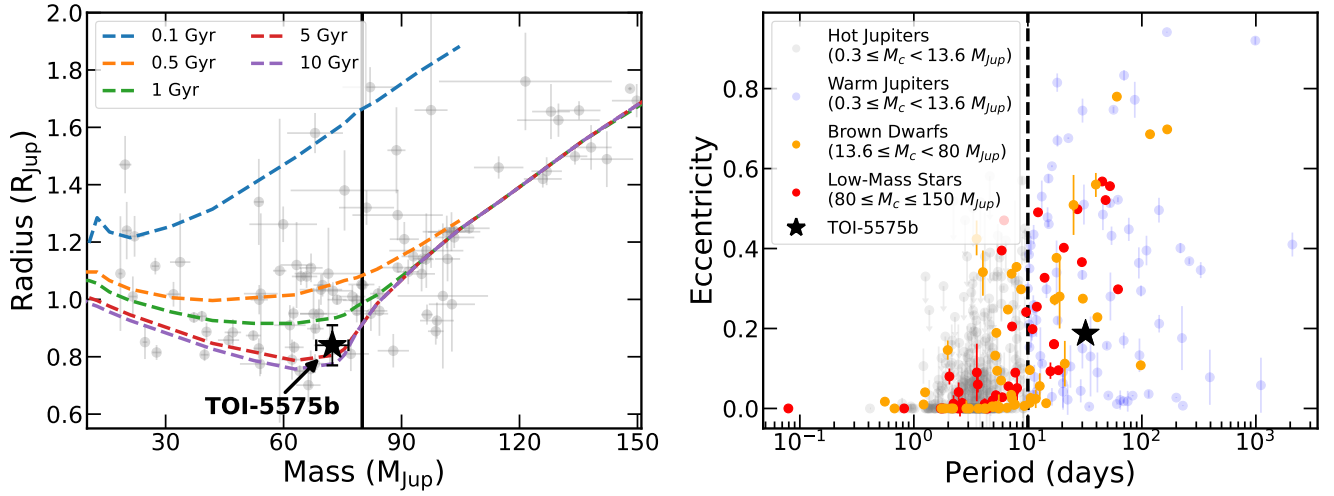


Figure 2. *Left panel:* The mass and radius diagram of all confirmed transiting brown dwarfs and low-mass stars. The colored dashed lines are the theoretical isochrones of cool brown dwarfs with different ages at solar metallicity from Baraffe et al. (2003). The vertical solid line marks the mass of $80 M_{\text{J}}$. *Right panel:* The eccentricity vs. orbital periods of known transiting brown dwarfs (orange) and low-mass stars (red). The vertical dashed line marks the 10-day period boundary that we used to select long-period objects for statistics. The blue dots are the selected transiting warm Jupiters while the transiting hot Jupiters are shown as gray dots for reference. In both panels, TOI-5575b is shown as a black star.

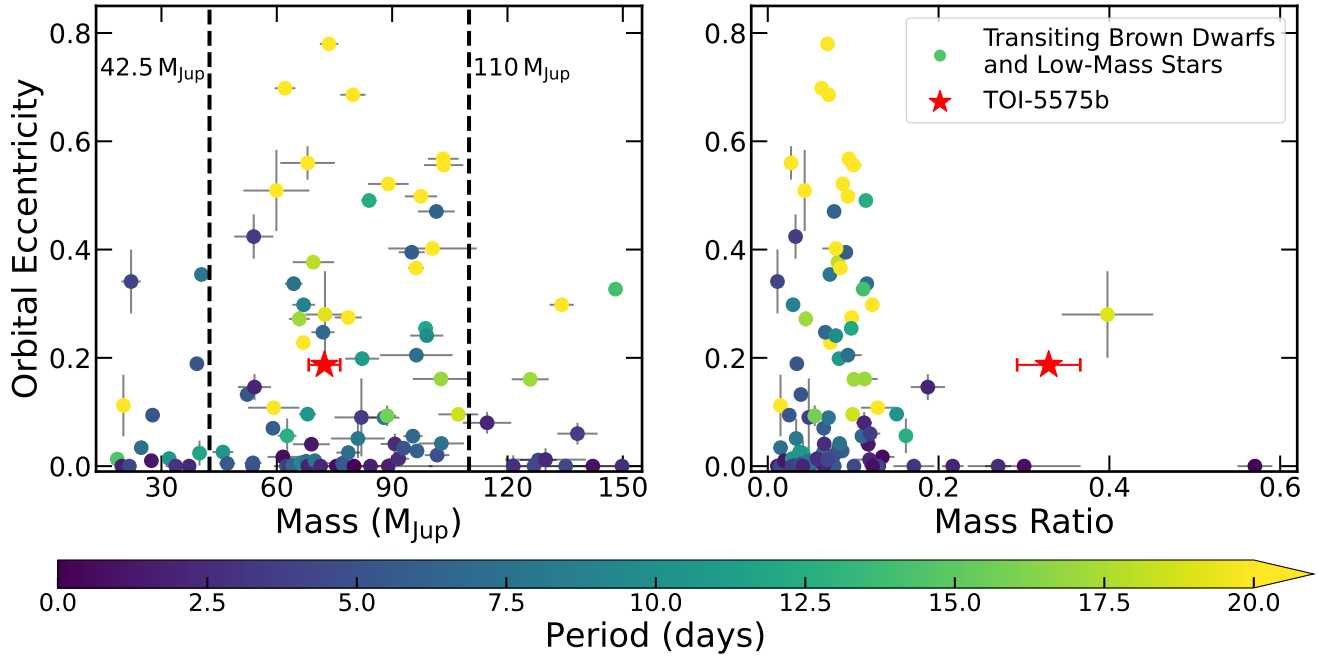


Figure 3. *Left panel:* The eccentricity and mass diagram of all confirmed transiting brown dwarfs and low-mass stars colored by the orbital period. Two vertical black dashed lines mark the mass range ($42.5 \leq M_c \leq 110 M_{\text{J}}$) where the companions are more likely to have large eccentricities (see Section 3.3 for details). *Right panel:* Same to the left but for the companion-to-host mass ratio. In both panels, TOI-5575b is shown as a red star.

TOI-5575b system reported in this work. We emphasize that all companions in the list are transiting systems, and therefore have true mass measurements. We limit our brown dwarf population to companions with masses between 13.6 and 80 M_J , and filter out low-mass star systems that have companion masses $80 \leq M_c \leq 150 M_J$. We exclude short-period systems and only accept objects with $10 \leq P \lesssim 1000$ days (corresponding to a semi-major axis range about 0.1-1.5 AU) to minimize the impact of stellar tidal effect that could erase the orbital eccentricity (see the eccentricity and period diagram in Figure 2). The inner period boundary is selected based on the tidal circularization timescale τ_{circ} . Assuming that the modified quality factors of a brown dwarf (Q_{BD}) and its host star (Q_*) both as typical values 10^6 (Goldreich & Soter 1966; Jackson et al. 2008), a brown dwarf with mass between 13-80 M_J and a period of 10 days orbiting a Sun-like star has a tidal circularization timescale τ_{circ} between 18 and 84 Gyrs using Equation 1 in Jackson et al. (2008), which we treat as unaffected by tidal effects. Eventually, a total of 19 brown dwarfs and 15 low-mass stars are left in our sample. We list all their properties in Table 3.

Our warm Jupiter sample is retrieved from the NASA Exoplanet Archive⁴ (Akeson et al. 2013). We preselect planets that have radius (i.e., transiting) and eccentricity measurements with mass over 0.3 M_J but smaller than 13.6 M_J and the same orbital period boundary as above, leading to 94 systems in total. We threw out 11 warm Jupiters that only have mass upper limits, most of which are mainly due to small RV amplitudes but large RV scatters. We also restrict the sample to systems with determined eccentricities instead of upper limits, and we further exclude 5 systems. In the end, our warm Jupiter sample consists of 78 planets. While the exclusion of objects with eccentricity upper limits could potentially bias toward higher eccentricities, we note that the number of excluded systems is small compared with the total sample size, and that they will not impact our conclusion significantly.

4.2. Modeling the Eccentricity Distribution

We opt to characterize the eccentricity distribution of the transiting long-period giant planet, brown dwarf and low-mass star categories using the Beta distribution, which has been widely used in many previous works (e.g., Hogg et al. 2010; Kipping 2013; Van Eylen et al. 2019; Stevenson et al. 2025). The choice of Beta distribution is motivated by the following two reasons: it

is intrinsically defined over the range 0 and 1, and it can produce probability density functions with various shapes using only two parameters. The standard Beta distribution is formulated as:

$$f(e; \alpha, \beta) = \frac{\Gamma(\alpha + \beta)e^{\alpha-1}(1-e)^{\beta-1}}{\Gamma(\alpha)\Gamma(\beta)}, \quad (1)$$

where e is the orbital eccentricity, Γ represents the gamma function, α and β are two parameters that determine the shape of the Beta distribution (Kipping 2013), so-called the shape parameters.

To properly account for measurement uncertainties, we implement a Monte Carlo resampling approach. We resample the eccentricity of each system by randomly drawing samples, assuming truncated Gaussian distributions $\mathcal{TN}(e, \sigma_e^2, 0, 1)$. Thanks to the large RV amplitudes, the eccentricities of most objects in our sample are precisely determined and the majority of eccentricity uncertainties are at the level of $\lesssim 0.1$, with a median error of 0.023, 0.006 and 0.003 for giant planets, brown dwarfs and low-mass stars, respectively. For those measurements that have different upper and lower errors, we adopt the larger one as σ_e in order to be conservative. We loop the procedure for 2,000 times for every system, hence we have 2,000 synthetic datasets. We utilize the Beta distribution function embedded in the `Scipy` package (Virtanen et al. 2020) to perform the fit through the least χ^2 method, and record all best-fit shape parameter pairs. We randomly select 30 synthetic datasets and the corresponding best Beta distribution fits, and we validate that these results match with observations.

Figure 4 shows the best-fit probability density functions of three companion groups. Giant planets and brown dwarfs with periods longer than 10 days have almost identical eccentricity distributions, preferring circular orbits with an extended tail toward high eccentricities. In the right panel of Figure 4, we present the resulting shape parameter distributions of all 2,000 simulated datasets of giant planets and brown dwarfs, which overlap with each other within about 1σ . The best-fitting shape parameters of the giant planet sample are $\alpha = 0.64_{-0.06}^{+0.07}$ and $\beta = 1.55_{-0.10}^{+0.12}$ while the results of brown dwarfs are $\alpha = 0.78_{-0.12}^{+0.08}$ and $\beta = 1.80_{-0.20}^{+0.15}$. In contrast, low-mass stars within the same period range have a remarkably different behavior ($\alpha = 2.42_{-0.13}^{+0.12}$ and $\beta = 5.12_{-0.22}^{+0.20}$), which tend to have moderate eccentricities peaking at about 0.3. Finally, by visual inspection, we note that long-period giant planets and brown dwarfs are more likely to have highly eccentric orbits with $e > 0.6$ compared with low-mass stars. In fact, all 15 companions in our low-mass star sample have eccentricities below 0.6 while there are 3 of 19 (15.8%) brown

⁴ <https://exoplanetarchive.ipac.caltech.edu>

Table 3. Properties of the transiting long-period brown dwarf and low-mass star sample^[1]

Object	Period [d]	M_2 [M_J]	R_2 [R_J]	Eccentricity	M_1 [M_\odot]	R_1 [R_\odot]	T_{eff} [K]	[Fe/H]
<i>Brown Dwarfs</i> (19 in total):								
TOI-1278b	14.48	$18.50^{+0.50}_{-0.50}$	$1.09^{+0.24}_{-0.20}$	$0.013^{+0.004}_{-0.004}$	$0.54^{+0.02}_{-0.02}$	$0.57^{+0.01}_{-0.01}$	3799^{+42}_{-42}	$-0.01^{+0.28}_{-0.28}$
Kepler-39b	21.09	$20.10^{+1.30}_{-1.20}$	$1.24^{+0.09}_{-0.10}$	$0.112^{+0.057}_{-0.057}$	$1.29^{+0.06}_{-0.07}$	$1.40^{+0.10}_{-0.10}$	6350^{+100}_{-100}	$0.10^{+0.14}_{-0.14}$
TOI-4776b	10.41	$32.00^{+1.90}_{-1.80}$	$1.02^{+0.05}_{-0.04}$	$0.014^{+0.023}_{-0.010}$	$1.06^{+0.07}_{-0.07}$	$1.22^{+0.46}_{-0.40}$	6011^{+33}_{-33}	$-0.05^{+0.05}_{-0.05}$
KOI-205b ^[2]	11.72	$39.90^{+1.00}_{-1.00}$	$0.81^{+0.02}_{-0.02}$	$0.024^{+0.023}_{-0.023}$	$0.93^{+0.03}_{-0.03}$	$0.84^{+0.02}_{-0.02}$	5237^{+60}_{-60}	$0.14^{+0.12}_{-0.12}$
TOI-1406b	10.57	$46.00^{+2.60}_{-2.70}$	$0.86^{+0.03}_{-0.03}$	$0.026^{+0.013}_{-0.010}$	$1.18^{+0.08}_{-0.09}$	$1.35^{+0.03}_{-0.03}$	6290^{+100}_{-100}	$-0.08^{+0.09}_{-0.09}$
RIK 72b	97.76	$59.20^{+6.80}_{-6.70}$	$3.10^{+0.31}_{-0.31}$	$0.108^{+0.012}_{-0.006}$	$0.44^{+0.04}_{-0.04}$	$0.96^{+0.10}_{-0.10}$	3349^{+142}_{-142}	$0.00^{+0.10}_{-0.10}$
TOI-811b	25.17	$59.90^{+13.00}_{-8.60}$	$1.26^{+0.06}_{-0.06}$	$0.509^{+0.075}_{-0.075}$	$1.32^{+0.05}_{-0.07}$	$1.27^{+0.06}_{-0.09}$	6107^{+77}_{-77}	$0.40^{+0.07}_{-0.09}$
KOI-415b	166.79	$62.14^{+2.69}_{-2.69}$	$0.79^{+0.12}_{-0.07}$	$0.698^{+0.002}_{-0.002}$	$0.94^{+0.06}_{-0.06}$	$1.25^{+0.15}_{-0.10}$	5810^{+80}_{-80}	$-0.24^{+0.11}_{-0.11}$
LHS 6343b	12.71	$62.70^{+2.40}_{-2.40}$	$0.83^{+0.02}_{-0.02}$	$0.056^{+0.032}_{-0.032}$	$0.37^{+0.01}_{-0.01}$	$0.38^{+0.01}_{-0.01}$	3130^{+20}_{-20}	$0.04^{+0.08}_{-0.08}$
TOI-1982b	17.17	$65.85^{+2.75}_{-2.72}$	$1.08^{+0.04}_{-0.04}$	$0.272^{+0.014}_{-0.014}$	$1.41^{+0.08}_{-0.08}$	$1.51^{+0.05}_{-0.05}$	6325^{+110}_{-110}	$-0.10^{+0.09}_{-0.09}$
EPIC 201702477b	40.74	$66.90^{+1.70}_{-1.70}$	$0.76^{+0.07}_{-0.07}$	$0.228^{+0.003}_{-0.003}$	$0.87^{+0.03}_{-0.03}$	$0.90^{+0.06}_{-0.06}$	5517^{+70}_{-70}	$-0.16^{+0.05}_{-0.05}$
HIP 33609b	39.47	$68.00^{+7.40}_{-7.10}$	$1.58^{+0.07}_{-0.07}$	$0.560^{+0.029}_{-0.031}$	$2.38^{+0.10}_{-0.10}$	$1.86^{+0.09}_{-0.08}$	10400^{+800}_{-660}	$-0.01^{+0.19}_{-0.20}$
TOI-5389Ab	10.40	$68.00^{+2.20}_{-2.20}$	$0.78^{+0.04}_{-0.03}$	$0.096^{+0.003}_{-0.005}$	$0.43^{+0.02}_{-0.02}$	$0.42^{+0.02}_{-0.02}$	3569^{+59}_{-59}	$-0.15^{+0.16}_{-0.16}$
NGTS-19b	17.84	$69.50^{+5.70}_{-5.40}$	$1.03^{+0.06}_{-0.05}$	$0.377^{+0.006}_{-0.006}$	$0.81^{+0.04}_{-0.04}$	$0.90^{+0.04}_{-0.04}$	4716^{+39}_{-28}	$0.11^{+0.07}_{-0.07}$
TOI-5575b (This Work)	32.07	$72.40^{+4.10}_{-4.10}$	$0.84^{+0.07}_{-0.07}$	$0.187^{+0.002}_{-0.002}$	$0.21^{+0.02}_{-0.02}$	$0.24^{+0.02}_{-0.02}$	3115^{+100}_{-100}	$-0.21^{+0.07}_{-0.07}$
TOI-6508b	18.99	$72.53^{+7.61}_{-5.09}$	$1.03^{+0.03}_{-0.03}$	$0.280^{+0.090}_{-0.080}$	$0.17^{+0.02}_{-0.02}$	$0.20^{+0.01}_{-0.01}$	3003^{+71}_{-69}	$-0.22^{+0.08}_{-0.08}$
TOI-2490b	60.33	$73.60^{+2.40}_{-2.40}$	$1.00^{+0.02}_{-0.02}$	$0.7799^{+0.0005}_{-0.0005}$	$1.00^{+0.03}_{-0.02}$	$1.10^{+0.01}_{-0.01}$	5558^{+80}_{-80}	$0.32^{+0.05}_{-0.05}$
KOI-189b	30.36	$78.60^{+3.50}_{-3.50}$	$1.00^{+0.02}_{-0.02}$	$0.275^{+0.004}_{-0.004}$	$0.76^{+0.05}_{-0.05}$	$0.73^{+0.02}_{-0.02}$	4952^{+40}_{-40}	$-0.12^{+0.10}_{-0.10}$
Kepler-807b	117.93	$79.80^{+3.40}_{-3.30}$	$1.05^{+0.51}_{-0.49}$	$0.686^{+0.002}_{-0.002}$	$1.07^{+0.07}_{-0.07}$	$1.20^{+0.05}_{-0.04}$	5994^{+78}_{-78}	$0.04^{+0.06}_{-0.05}$
<i>Low-Mass Stars</i> (15 in total):								
TOI-746B	10.98	$82.20^{+4.90}_{-4.40}$	$0.95^{+0.09}_{-0.06}$	$0.199^{+0.003}_{-0.003}$	$0.94^{+0.09}_{-0.08}$	$0.97^{+0.04}_{-0.03}$	5690^{+140}_{-140}	$-0.02^{+0.23}_{-0.23}$
TOI-4635B	12.28	$84.00^{+2.10}_{-2.00}$	$1.02^{+0.02}_{-0.02}$	$0.491^{+0.002}_{-0.002}$	$0.70^{+0.03}_{-0.03}$	$0.68^{+0.01}_{-0.01}$	4555^{+67}_{-74}	$-0.09^{+0.04}_{-0.03}$
TOI-681B	15.78	$88.70^{+2.50}_{-2.30}$	$1.52^{+0.25}_{-0.15}$	$0.093^{+0.022}_{-0.019}$	$1.54^{+0.06}_{-0.05}$	$1.47^{+0.04}_{-0.04}$	7440^{+150}_{-140}	$-0.08^{+0.05}_{-0.05}$
TOI-694B	48.05	$89.00^{+5.30}_{-5.30}$	$1.11^{+0.02}_{-0.02}$	$0.521^{+0.002}_{-0.002}$	$0.97^{+0.05}_{-0.04}$	$1.00^{+0.01}_{-0.01}$	5496^{+87}_{-81}	$0.21^{+0.08}_{-0.08}$
TIC 320687387B	29.77	$96.20^{+1.90}_{-2.00}$	$1.14^{+0.02}_{-0.02}$	$0.366^{+0.003}_{-0.003}$	$1.08^{+0.03}_{-0.03}$	$1.16^{+0.02}_{-0.02}$	5780^{+80}_{-80}	$0.30^{+0.08}_{-0.08}$
TOI-1213B	27.22	$97.50^{+4.40}_{-4.20}$	$1.66^{+0.78}_{-0.55}$	$0.498^{+0.003}_{-0.002}$	$0.99^{+0.07}_{-0.06}$	$0.99^{+0.04}_{-0.04}$	5590^{+150}_{-150}	$0.25^{+0.13}_{-0.14}$
K2-76B	11.99	$98.70^{+1.99}_{-1.99}$	$0.89^{+0.03}_{-0.03}$	$0.255^{+0.007}_{-0.006}$	$0.96^{+0.03}_{-0.03}$	$1.17^{+0.03}_{-0.06}$	5747^{+64}_{-70}	$0.01^{+0.04}_{-0.04}$
CoRoT 101186644B	20.68	$100.50^{+11.50}_{-11.50}$	$1.01^{+0.06}_{-0.25}$	$0.402^{+0.006}_{-0.006}$	$1.20^{+0.20}_{-0.20}$	$1.07^{+0.07}_{-0.07}$	6090^{+200}_{-200}	$0.20^{+0.20}_{-0.20}$
BD+29 4980B	16.95	$102.70^{+7.33}_{-7.33}$	$1.24^{+0.07}_{-0.07}$	$0.161^{+0.002}_{-0.003}$	$0.86^{+0.10}_{-0.10}$	$0.85^{+0.05}_{-0.06}$	5150^{+90}_{-90}	$0.10^{+0.14}_{-0.14}$
EBLM J2114-39B	44.92	$103.29^{+3.98}_{-3.98}$	$1.24^{+0.02}_{-0.02}$	$0.5677^{+0.0005}_{-0.0004}$	$1.04^{+0.06}_{-0.06}$	$1.28^{+0.02}_{-0.02}$	5763^{+216}_{-216}	$-0.03^{+0.14}_{-0.14}$
KOI-686B	52.51	$103.40^{+5.10}_{-5.10}$	$1.22^{+0.04}_{-0.04}$	$0.556^{+0.004}_{-0.004}$	$0.98^{+0.07}_{-0.07}$	$1.04^{+0.03}_{-0.03}$	5834^{+100}_{-100}	$-0.06^{+0.13}_{-0.13}$
TIC 220568520B	18.56	$107.20^{+5.20}_{-5.20}$	$1.25^{+0.02}_{-0.02}$	$0.096^{+0.003}_{-0.003}$	$1.03^{+0.04}_{-0.04}$	$1.01^{+0.01}_{-0.01}$	5589^{+81}_{-81}	$0.26^{+0.07}_{-0.07}$
EBLM J2343+29B	16.95	$125.92^{+4.82}_{-4.82}$	$1.42^{+0.03}_{-0.03}$	$0.1604^{+0.0003}_{-0.0003}$	$1.19^{+0.07}_{-0.07}$	$0.91^{+0.02}_{-0.02}$	4984^{+87}_{-87}	$0.11^{+0.05}_{-0.05}$
TIC 231005575B	61.78	$134.10^{+3.14}_{-3.14}$	$1.50^{+0.03}_{-0.03}$	$0.298^{+0.004}_{-0.001}$	$1.04^{+0.04}_{-0.04}$	$0.99^{+0.05}_{-0.05}$	5500^{+85}_{-85}	$-0.44^{+0.06}_{-0.06}$
KIC 1571511B	14.02	$148.10^{+0.53}_{-0.53}$	$1.74^{+0.00}_{-0.01}$	$0.327^{+0.003}_{-0.003}$	$1.26^{+0.04}_{-0.03}$	$1.34^{+0.01}_{-0.01}$	6195^{+50}_{-50}	$0.37^{+0.08}_{-0.08}$

[1] This catalog is built by combining the lists published in Vowell et al. (2025) and Barkaoui et al. (2025) as well as a few recent discoveries (Larsen et al. 2025; Zhang et al. 2025). [2] The orbital eccentricity of KOI-205b reported in the reference Diaz et al. (2013) is an upper limit (< 0.031). Here, the result $e = 0.024 \pm 0.023$ is derived based on our independent fit using the same RV dataset.

dwarfs and 10 of 78 (12.8%) warm Jupiters above this limit. Meanwhile, low-mass stars with circular orbits seem to be rare. The fractions of objects in our sample with $e \leq 0.1$ are 29.5%, 31.6% and 13.3% for giant planets, brown dwarfs and low-mass stars, respectively.

Since a more fundamental parameter related to the tidal circularization timescale is scaled semi-major axis, we repeat our analysis by selecting transiting long-period companions with a/R_* instead. We investigate three different cuts: $a/R_* \geq 10$, $a/R_* \geq 15$ and $a/R_* \geq 20$, and we perform the same Beta distribution fit as described above. The results are presented in Figure 5. We find that transiting long-period giant planets and brown dwarfs always prefer low eccentricities in all cases with similar eccentricity distributions,

agreeing with our conclusion using the orbital period cut. The low-mass stars, however, only show an eccentricity peak at about 0.3 when we use the $a/R_* \geq 15$ and $a/R_* \geq 20$ cuts. We suspect that tidal effect may play a role in circularizing the orbits of some companions with $10 < a/R_* < 15$.

5. DISCUSSIONS

5.1. Comparison to Wide-Orbit Cold Worlds

Based on a sample of transiting long-period giant planets, brown dwarfs and low-mass stars with $10 \leq P \lesssim 1000$ days, we find that 1) the eccentricity distribution of giant planets resembles that of brown dwarfs; 2) the eccentricity distribution of low-mass stars is distinct from the other two populations with a peak at about

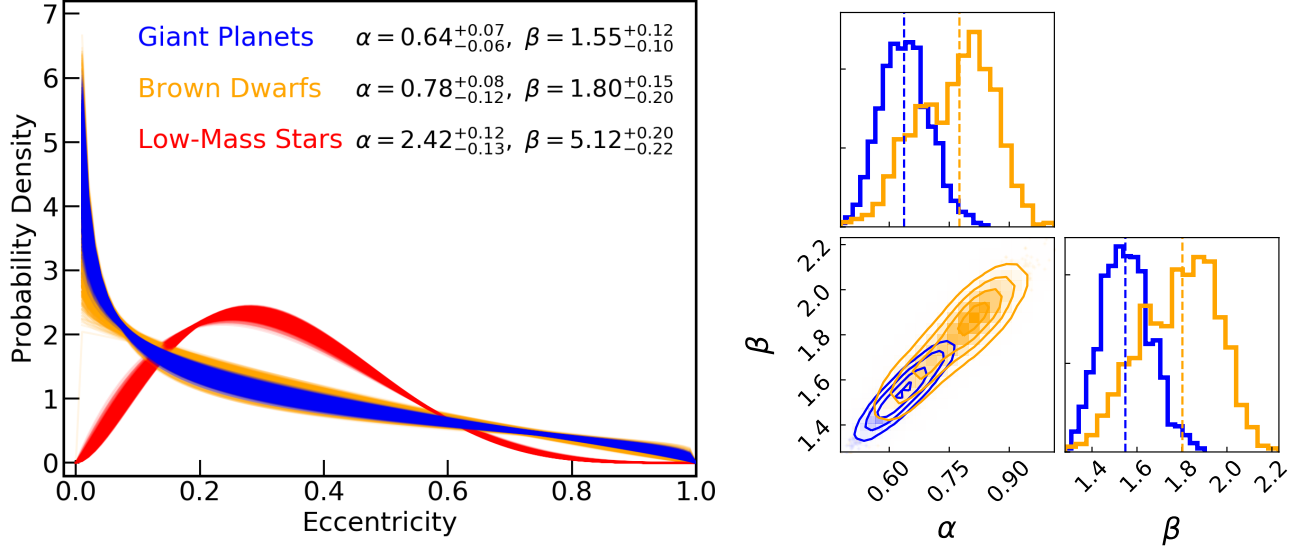


Figure 4. *Left panel:* The best-fit eccentricity distributions of 2,000 randomly generated eccentricity data sets of transiting long-period ($10 \leq P \lesssim 1000$ days) giant planets (blue, $M_c < 13.6 M_J$), brown dwarfs (orange, $13.6 \leq M_c < 80 M_J$) and low-mass stars (red, $80 \leq M_c \leq 150 M_J$), assuming truncated Gaussian distributions (see Section 4.2 for details). The best-fit shape parameters of the Beta distribution (Equation 1) are shown on the top right. *Right panel:* The distribution of best-fit shape parameter pairs of 2,000 simulated data sets of giant planets (blue) and brown dwarfs (orange), consistent with each other within about 1σ . The vertical dashed lines show the best-fit parameters. The eccentricity distributions of transiting long-period brown dwarfs are similar to giant planets but different from low-mass stars.

0.3. Using scaled semi-major axis ($a/R_* \geq 10, 15, 20$) instead to select the transiting long-period samples, we find that the conclusions do not change except that the peak at about 0.3 in the eccentricity distribution of low-mass stars disappears when we apply the $a/R_* \geq 10$ cut (Figure 5), which we attribute to tidal circularization. The semi-major axis range of our sample is roughly 0.1–1.5 AU. Therefore, our results complement the previous studies from Bowler et al. (2020), Nagpal et al. (2023) and Do Ó et al. (2023), who investigate the eccentricities of cold giants and brown dwarf companions detected by direct imaging. All works reported that the underlying eccentricity distributions of imaged cold gas giants and brown dwarfs within the semi-major axis range 5–100 AU are significantly different: cold brown dwarfs have a broad eccentricity distribution with a peak locating at 0.6–0.9 while imaged gas giants prefer a lower eccentricity around 0.05–0.25 (see Figure 19 and 20 in Bowler et al. 2020). By performing a similar Beta distribution analysis, Bowler et al. (2020) found that the best-fit shape parameters of cold giant planets and brown dwarfs are $[\alpha \approx 30, \beta \approx 200]$ and $[\alpha \approx 2.3, \beta \approx 1.65]$, respectively. Interestingly, the eccentricity distribution of inner giant planets and brown dwarfs studied in this work are notably different from outer cold ones. We put forward two possible hypotheses to explain such a discrepancy.

The first scenario is straightforward: warm Jupiters and brown dwarfs went through a similar evolution history. Under this framework, both giant planets and brown dwarfs initially form far away from the hosts in two different channels, as suggested by Bowler et al. (2020), resulting in different eccentricity distributions. Specifically, giant planets might generate from core accretion, which tends to induce low orbital eccentricities while brown dwarfs predominantly form by gravitational instability in massive disks that could inherit higher eccentricities. Subsequently, cold giant planets and brown dwarfs experience similar dynamic evolutions such as companion-disk interaction and companion-companion scattering (Alqasim et al. 2025), leading to analogous eccentricity distributions we finally saw in Figure 4.

The second hypothesis is that the eccentricity distributions of inner gas giants and brown dwarfs are jointly shaped by two different sub-groups. Similar as the previous scenario, the giant planets and brown dwarfs were born at exterior orbits with different eccentricity distributions. During the migration to inner orbits with $10 \leq P \lesssim 1000$ days, some giant planets may remain dynamically stable all the time and preserve small eccentricities (Teyssandier & Lai 2020) while a part of them undergo orbital instability through scattering, leaving diverse eccentricities (Ida et al. 2013). The superposition of these two sub-groups yields the final eccentricity

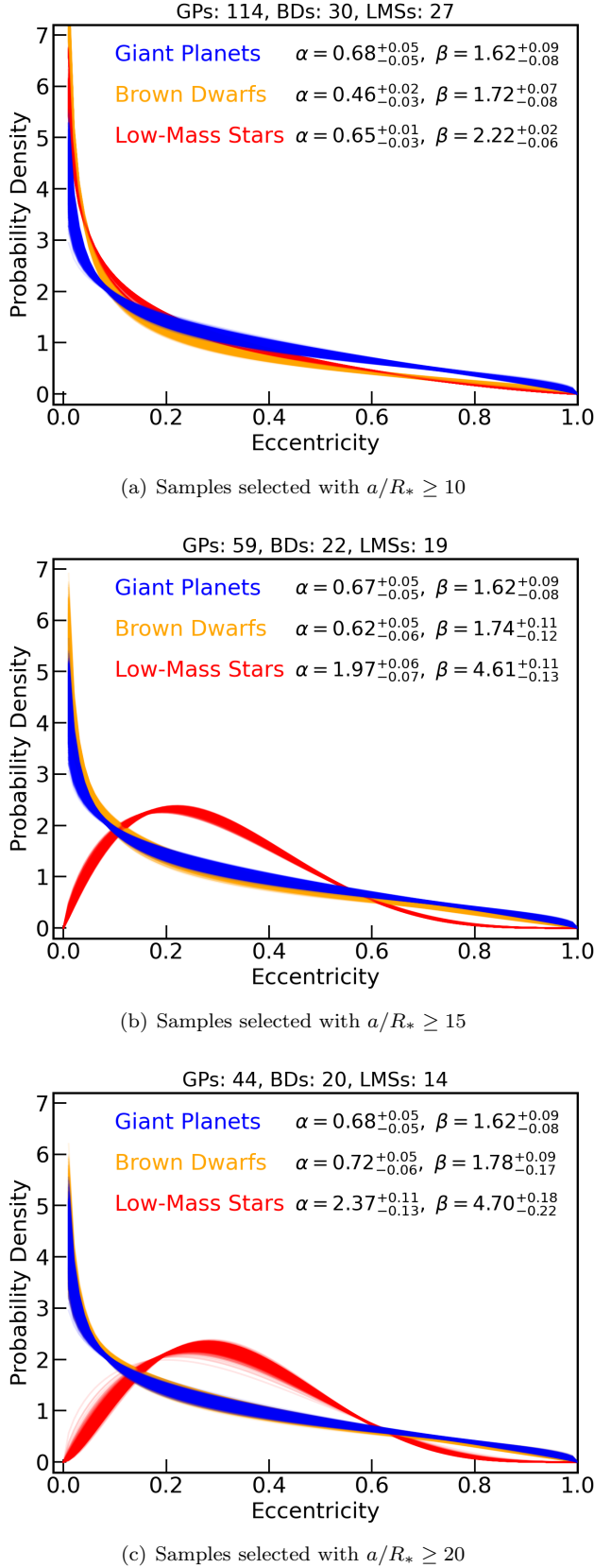


Figure 5. Same as Figure 4 but using a/R_* to select long-period systems. From top to bottom, they are results using $a/R_* \geq 10$, $a/R_* \geq 15$ and $a/R_* \geq 20$. The number of companions in each group is shown in the title of each panel.

distribution seen in Figure 4. Regarding the cold giant planets detected via direct imaging, they seem to prefer low-eccentricity orbits (Bowler et al. 2020) because they probably do not encounter dynamically hot interactions after formation. In terms of brown dwarfs, considering that they originally formed through disk instability in the outer regions of massive disks, they tend to have high eccentricities at the beginning with a tentative peak at about 0.6–0.9, a feature seen in the direct imaging results (Bowler et al. 2020). However, their semi-major axes and eccentricities might be damped through dynamical friction with the disk since the formed brown dwarfs are sufficiently less massive than the disk (Ida et al. 2020). After migrating inwards to orbits with $10 \leq P \lesssim 1000$ days, some brown dwarfs may still keep the high eccentricities inherited during formation while the others have damped low eccentricities. A combination of these two brown dwarf subgroups ultimately produces the eccentricity distribution in Figure 4. Under this framework, the eccentricities of long-period giant planets and brown dwarfs with $10 \leq P \lesssim 1000$ days have similar distributions by coincident since they are actually shaped by different formation and evolution mechanisms.

Finally, it should also be mentioned that the low-mass stars in our sample have a peak eccentricity around 0.3. Such a feature has also been observed in radial velocity surveys decades ago (e.g., Duquennoy & Mayor 1991) and recent astrometry studies (e.g., Wu et al. 2025) for more massive wide binaries. The results hint that the evolution of low-mass stars is probably similar to massive stellar binary systems. However, the origin of the peak at about 0.3 in the eccentricity distribution is still unclear. Theoretical works suggest that the orbits of binary systems could be excited by circumbinary disks (Tokovinin & Moe 2020; Lai & Muñoz 2023; Siwek et al. 2023) and reach a high eccentricity at about 0.3, depending on intrinsic properties of the system such as mass ratio (Valli et al. 2024). In the meantime, multi components like outer massive companion (Eggleton & Kisseleva-Eggleton 2006; Fabrycky & Tremaine 2007; Naoz & Fabrycky 2014) as well as flyby encounters (Heggie & Rasio 1996) should not be neglected, both of which could excite orbits. More recently, Wu et al. (2025) proposed that the eccentricity peak of close stellar binaries at about 0.3 could also be due to the ejection of brown dwarf objects.

5.2. Future Prospects

The number of transiting long-period brown dwarfs and low-mass stars, particularly those have periods $P > 100$ days with true mass measured (see Figure 2), are

still limited. Despite that, the Gaia DR4 and DR5 shall remedy the situation. Through the astrometry method, one could determine the true companion mass and the orbital eccentricity simultaneously (e.g., Gan 2023; Stefánsson et al. 2025). In fact, numerous of astrometric binary stars and sub-stellar objects have already been released (Halbwachs et al. 2023; Holl et al. 2023). A larger sample will enable further exploration of the eccentricity trends of different stellar types, metallicities, periods, companion masses, etc, allowing for a more comprehensive mapping of eccentricity distribution and a more detailed comparison with predictions from different theories.

Additionally, different dynamical origins of brown dwarfs are supposed to leave specific signatures on the stellar obliquities. Dynamically violent interactions such as high-eccentricity migration may cause misalignment between the orbital angular momentum axis of the companion and the spin axis of the host star. Instead, we expect to observe well-aligned systems with low obliquities if they move inwards via quiescent processes like disk migration. To date, only eight brown dwarf systems have their obliquity measured (Triaud et al. 2009; Siverd et al. 2012; Triaud et al. 2013; Zhou et al. 2019; Ferreira dos Santos et al. 2024; Giacalone et al. 2024; Brady et al. 2025; Doyle et al. 2025), and all of them are short-period ($P < 10$ days) systems and are consistent with aligned orbits within about 1σ , hinting a dynamically quiet history. Consequently, it is crucial to enlarge this small sample and extend it to long-period brown dwarfs to further understand the evolution of such systems.

6. CONCLUSIONS

In this paper, we report the discovery of TOI-5575b, a long-period brown dwarf transiting a low-mass M5V star confirmed by space and ground photometric, spectroscopic and imaging observations. The brown dwarf companion has a mass of $72.4 \pm 4.1 M_J$ and a radius of $0.84 \pm 0.07 R_J$ with a period of about 32 days on an eccentric orbit ($e = 0.187 \pm 0.002$). Putting TOI-5575b into a broader context, we find that the majority of eccentric brown dwarfs and low-mass stars with $e > 0.3$ have mass between 42.5 and 110 M_J with orbital periods greater than 10 days.

We further compare the eccentricities of transiting long-period giant planets ($0.3 \leq M_c < 13.6 M_J$), brown dwarfs ($13.6 \leq M_c < 80 M_J$) and low-mass stars ($80 \leq M_c \leq 150 M_J$) with orbital periods $10 \leq P \lesssim 1000$ days (about 0.1-1.5 AU). We summarize our findings below.

- (i) The eccentricity distributions of transiting long-period giant planets and brown dwarfs are almost identical ($\alpha = 0.64^{+0.07}_{-0.06}$ and $\beta = 1.55^{+0.12}_{-0.10}$ for giant

planets, $\alpha = 0.78^{+0.08}_{-0.12}$ and $\beta = 1.80^{+0.15}_{-0.20}$ for brown dwarfs): both favoring low-eccentricity orbits with a long tail toward high eccentricities.

- (ii) Inner giant planets and brown dwarfs we studied in this work have eccentricity behaviors significantly different from outer cold counterparts within 5-100 AU detected by the direct imaging method ($\alpha \approx 30$ and $\beta \approx 200$ for imaged giant planets, $\alpha \approx 2.30$ and $\beta \approx 1.65$ for imaged brown dwarfs), where brown dwarfs show a broad eccentricity distribution with a peak locating at 0.6-0.9 but giant planets display a preference for low eccentricities between 0.05 and 0.25 (Bowler et al. 2020).
- (iii) Unlike the giant planet and brown dwarf population, transiting low-mass stars show a peak eccentricity at about 0.3 ($\alpha = 2.42^{+0.12}_{-0.13}$ and $\beta = 5.12^{+0.20}_{-0.22}$), similar to more massive wide binary systems. Low-mass stars with circular orbits or highly eccentric orbits ($e > 0.6$) are rarer compared with the giant planets and brown dwarfs.

The similarity in the eccentricity distributions of transiting long-period giant planets and brown dwarfs might be due to a similar dynamical evolution history or both of them contain two sub-groups that jointly shape similar eccentricity distributions. A larger sample size and follow-up obliquity studies will enable more comprehensive insights.

7. ACKNOWLEDGMENTS

We thank the anonymous referee for the constructive comments that improve the quality of this work. We also thank Noah Vowell and Khalid Barkaoui for kindly sharing their brown dwarf and low-mass star catalogs, without which this work would not be possible. We are grateful to Doug Lin, Yanqin Wu and Dong Lai for the useful discussions on the eccentricities of brown dwarfs and binary systems as well as dynamical processes.

T.G. and S.M. acknowledge support by the National Natural Science Foundation of China (Grant No. 12133005). The work of I.A.S. was conducted under the state assignment of Lomonosov Moscow State University. Z.L.D. would like to thank the generous support of the MIT Presidential Fellowship, the MIT Collamore-Rogers Fellowship, and the MIT Teaching Development Fellowship and to acknowledge that this material is based upon work supported by the National Science Foundation Graduate Research Fellowship under Grant No. 1745302.

This research uses data obtained through the Telescope Access Program (TAP), which is funded by the

National Astronomical Observatories, Chinese Academy of Sciences, and the Special Fund for Astronomy from the Ministry of Finance. This work is partly supported by the Natural Science and Engineering Research Council of Canada, the Canadian Space Agency and the Trottier Family Foundation through their support of the Trottier Institute for Research on Exoplanets (IREx). This work benefited from support of the Fonds de recherche du Québec – Nature et technologies (FRQNT), through the Center for Research in Astrophysics of Quebec.

Based on observations obtained at the Canada-France-Hawaii Telescope (CFHT) which is operated from the summit of Maunakea by the National Research Council of Canada, the Institut National des Sciences de l’Univers of the Centre National de la Recherche Scientifique of France, and the University of Hawaii. The observations at the Canada-France-Hawaii Telescope were performed with care and respect from the summit of Maunakea which is a significant cultural and historic site. Based on observations obtained with SPIRou, an international project led by Institut de Recherche en Astrophysique et Planétologie, Toulouse, France.

Some of the observations in this paper made use of the High-Resolution Imaging instrument ‘Alopeke and were obtained under Gemini LLP Proposal Number: GN-2025A-DD-101. ‘Alopeke was funded by the NASA Exoplanet Exploration Program and built at the NASA Ames Research Center by Steve B. Howell, Nic Scott, Elliott P. Horch, and Emmett Quigley. Alopeke was mounted on the Gemini North telescope of the international Gemini Observatory, a program of NSF’s OIR Lab, which is managed by the Association of Universities

for Research in Astronomy (AURA) under a cooperative agreement with the National Science Foundation. on behalf of the Gemini partnership: the National Science Foundation (United States), National Research Council (Canada), Agencia Nacional de Investigación y Desarrollo (Chile), Ministerio de Ciencia, Tecnología e Innovación (Argentina), Ministério da Ciência, Tecnologia, Inovações e Comunicações (Brazil), and Korea Astronomy and Space Science Institute (Republic of Korea).

Funding for the TESS mission is provided by NASA’s Science Mission Directorate. We acknowledge the use of public TESS data from pipelines at the TESS Science Office and at the TESS Science Processing Operations Center. Resources supporting this work were provided by the NASA High-End Computing (HEC) Program through the NASA Advanced Supercomputing (NAS) Division at Ames Research Center for the production of the SPOC data products. This research has made use of the Exoplanet Follow-up Observation Program website, which is operated by the California Institute of Technology, under contract with the National Aeronautics and Space Administration under the Exoplanet Exploration Program. This paper includes data collected by the *TESS* mission, which are publicly available from the Mikulski Archive for Space Telescopes (MAST).

Facilities: TESS, CFHT/SPIRou, Keck II/NIRES, Gemini-North/‘Alopeke, SAI-2.5m, ASP-0.36m, Gaia, ZTF

Software: lightcurve (Lightcurve Collaboration et al. 2018), AstroImageJ (Collins et al. 2017), juliet (Espinoza et al. 2019), batman (Kreidberg 2015), radvel (Fulton et al. 2018), Scipy (Virtanen et al. 2020), corner (Foreman-Mackey 2016)

APPENDIX

A. NORMALIZED TESS LIGHT CURVES

Figure A1 shows the normalized and detrended TESS light curves of TOI-5575.

B. SPIROU RADIAL VELOCITIES

All SPIRou radial velocities we obtained for TOI-5575 are listed in Table B1.

C. THE KECK/NIRES SPECTRUM AND SED OF TOI-5575

Figure C1 shows the Keck/NIRES spectrum as well as broadband photometry of TOI-5575 along with the best-fit model.

D. SPECKLE IMAGING RESULTS

Figure D1 shows the speckle imaging results from SAI-2.5m and Gemini.

REFERENCES

- Akeson, R. L., Chen, X., Ciardi, D., et al. 2013, *PASP*, 125, 989, doi: [10.1086/672273](https://doi.org/10.1086/672273)
- Alqasim, A., Hirano, T., Hori, Y., et al. 2025, *MNRAS*, doi: [10.1093/mnras/staf418](https://doi.org/10.1093/mnras/staf418)

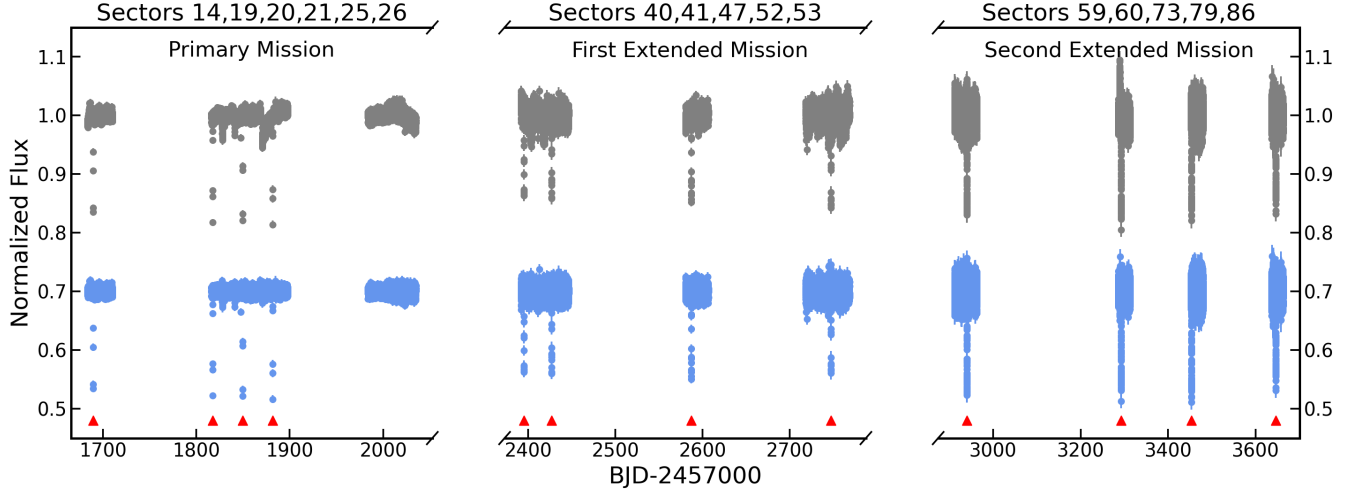


Figure A1. The normalized TESS light curves of TOI-5575. The left, middle and right panels are data from Primary, First and Second Extended Missions. The light curve from the Primary Mission was extracted with a 3×3 pixel box aperture while the light curves from the First and Second Extended Missions came from QLP and SPOC pipelines. The different transit depths seen in three panels are likely due to the different aperture sizes, resulting in different light dilutions. The raw light curves are shown above in gray while the detrended light curves are presented below in blue. The transits of TOI-5575b are marked with red triangles. The transit event in Sectors 25 and 26 happened during the data gaps so it does not show up.

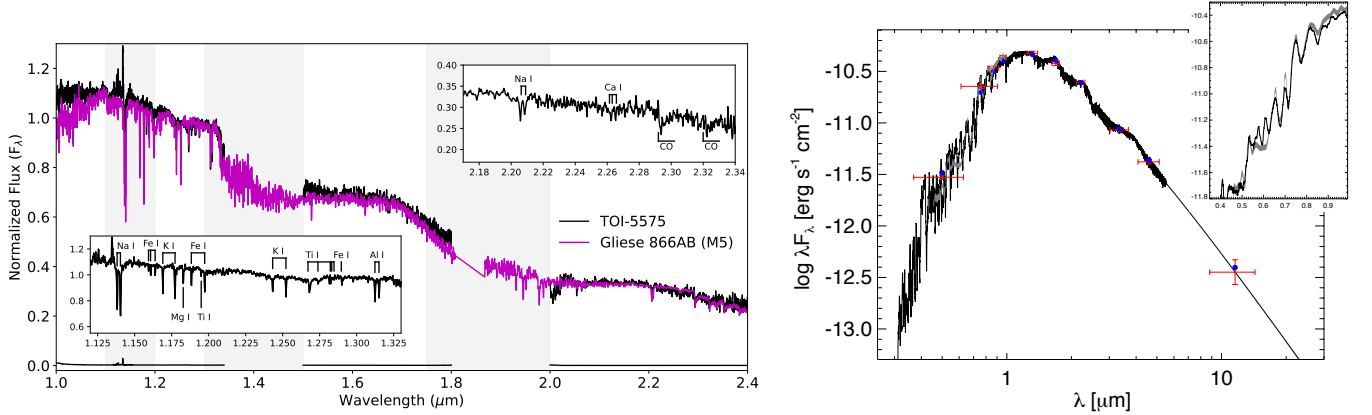


Figure C1. *Left panel:* Keck/NIRES spectrum of TOI-5575 (black line) compared to the equivalent data for the M5 standard Gliese 866AB (magenta line; Cushing et al. 2005). Both spectra are normalized at $1.3 \mu\text{m}$. Locations of major H_2O and CO molecular absorption bands are labeled, as are regions of strong telluric absorption (grey boxes, masked in spectrum of TOI-5575). The inset boxes show close-ups of the $1.12\text{--}1.33 \mu\text{m}$ and $2.18\text{--}2.34 \mu\text{m}$ regions with primary atomic and molecular features labeled. *Right panel:* The SED of TOI-5575. The red crosses are the observed photometric measurements, where the horizontal bars represent the effective width of the passband. All blue dots represent the model fluxes from the best-fit PHOENIX atmosphere model (black solid lines). The Gaia spectrum is shown as a gray swathe on the inset top right panel.

Artigau, É., Hébrard, G., Cadieux, C., et al. 2021, *AJ*, 162, 144, doi: [10.3847/1538-3881/ac096d](https://doi.org/10.3847/1538-3881/ac096d)
 Artigau, É., Cadieux, C., Cook, N. J., et al. 2022, *AJ*, 164, 84, doi: [10.3847/1538-3881/ac7ce6](https://doi.org/10.3847/1538-3881/ac7ce6)
 Baraffe, I., Chabrier, G., Barman, T. S., Allard, F., & Hauschildt, P. H. 2003, *A&A*, 402, 701, doi: [10.1051/0004-6361:20030252](https://doi.org/10.1051/0004-6361:20030252)
 Barkaoui, K., Sebastian, D., Zúñiga-Fernández, S., et al. 2025, *A&A*, 696, A44, doi: [10.1051/0004-6361/202453508](https://doi.org/10.1051/0004-6361/202453508)

Beaugé, C., & Nesvorný, D. 2012, *ApJ*, 751, 119, doi: [10.1088/0004-637X/751/2/119](https://doi.org/10.1088/0004-637X/751/2/119)
 Bellm, E. C., Kulkarni, S. R., Graham, M. J., et al. 2019, *PASP*, 131, 018002, doi: [10.1088/1538-3873/aaecbe](https://doi.org/10.1088/1538-3873/aaecbe)
 Benedict, G. F., Henry, T. J., Franz, O. G., et al. 2016, *AJ*, 152, 141, doi: [10.3847/0004-6256/152/5/141](https://doi.org/10.3847/0004-6256/152/5/141)
 Boss, A. P. 2000, *ApJL*, 536, L101, doi: [10.1086/312737](https://doi.org/10.1086/312737)
 Bowler, B. P., Blunt, S. C., & Nielsen, E. L. 2020, *AJ*, 159, 63, doi: [10.3847/1538-3881/ab5b11](https://doi.org/10.3847/1538-3881/ab5b11)

Table B1. Radial velocities measurements for TOI-5575 from SPIRou.

BJD	RV (m s ⁻¹)	σ_{RV} (m s ⁻¹)
2460065.995	-42867.1	16.8
2460066.009	-42881.0	17.5
2460067.997	-46980.4	25.2
2460068.012	-46946.8	39.8
2460072.960	-58244.1	16.7
2460072.974	-58238.5	17.0
2460074.957	-58835.2	16.8
2460074.972	-58773.4	17.1
2460076.988	-56064.7	21.6
2460077.002	-56009.5	21.7
2460096.888	-40897.2	26.0
2460096.902	-40904.2	29.5
2460098.911	-44622.0	22.2
2460098.926	-44586.1	22.1
2460101.898	-51580.8	22.8
2460101.912	-51605.9	24.7
2460103.887	-56373.3	15.2
2460103.901	-56369.3	15.2
2460123.826	-36998.1	17.7
2460123.840	-37004.1	17.2
2460124.871	-37266.9	16.9
2460124.885	-37248.2	16.6
2460125.861	-37773.0	19.4
2460125.875	-37772.1	20.4

Brady, M., Bean, J. L., Stefánsson, G., et al. 2025, *AJ*, 169, 64, doi: [10.3847/1538-3881/ad9c66](https://doi.org/10.3847/1538-3881/ad9c66)

Burgasser, A. J., Kirkpatrick, J. D., Reid, I. N., et al. 2003, *ApJ*, 586, 512, doi: [10.1086/346263](https://doi.org/10.1086/346263)

Carmichael, T. W., Irwin, J. M., Murgas, F., et al. 2022, *MNRAS*, 514, 4944, doi: [10.1093/mnras/stac1666](https://doi.org/10.1093/mnras/stac1666)

Carrera, D., Raymond, S. N., & Davies, M. B. 2019, *A&A*, 629, L7, doi: [10.1051/0004-6361/201935744](https://doi.org/10.1051/0004-6361/201935744)

Charbonneau, D., Allen, L. E., Megeath, S. T., et al. 2005, *ApJ*, 626, 523, doi: [10.1086/429991](https://doi.org/10.1086/429991)

Clark, C. A., van Belle, G. T., Horch, E. P., et al. 2024, *AJ*, 167, 56, doi: [10.3847/1538-3881/ad0bfd](https://doi.org/10.3847/1538-3881/ad0bfd)

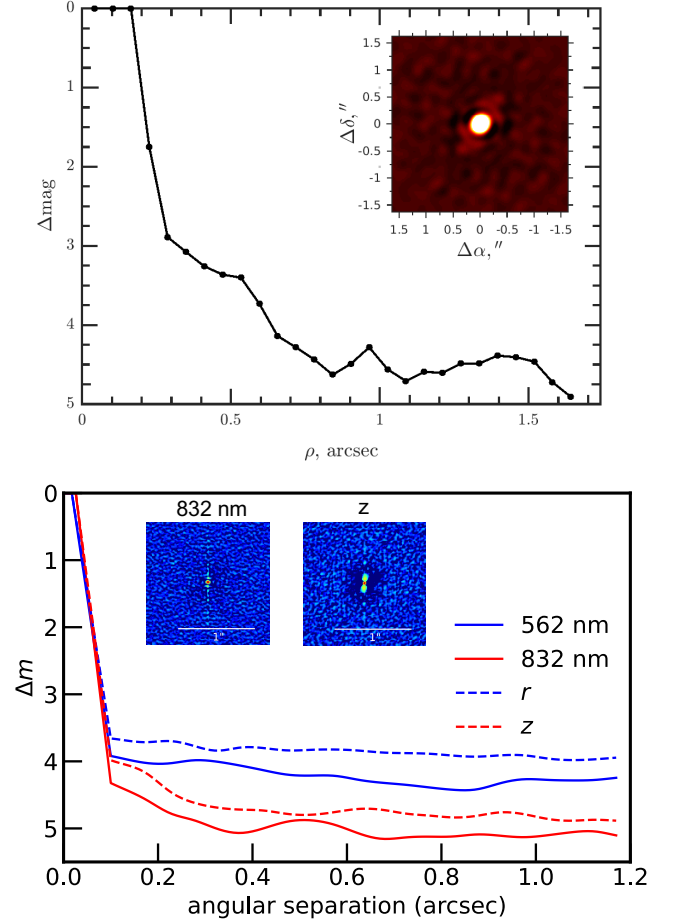
Collins, K. A., Kielkopf, J. F., Stassun, K. G., & Hessman, F. V. 2017, *AJ*, 153, 77, doi: [10.3847/1538-3881/153/2/77](https://doi.org/10.3847/1538-3881/153/2/77)

Cook, N. J., Artigau, É., Doyon, R., et al. 2022, *PASP*, 134, 114509, doi: [10.1088/1538-3873/ac9e74](https://doi.org/10.1088/1538-3873/ac9e74)

Cushing, M. C., Rayner, J. T., & Vacca, W. D. 2005, *ApJ*, 623, 1115, doi: [10.1086/428040](https://doi.org/10.1086/428040)

Cushing, M. C., Vacca, W. D., & Rayner, J. T. 2004, *PASP*, 116, 362, doi: [10.1086/382907](https://doi.org/10.1086/382907)

Cutri, R. M., Skrutskie, M. F., van Dyk, S., et al. 2003, 2MASS All Sky Catalog of point sources.

**Figure D1.** *Top panel:* Secondary component detection limits obtained using speckle imaging obtained with speckle polarimeter on the SAI-2.5m telescope. *Bottom panel:* Gemini high-resolution speckle imaging 5σ contrast limits as a function of angular separation. There are hints of a close companion in the reconstructed images, but these observations were taken at high airmass, and the orientation is consistent with the star being “smeared” along the parallactic angle, rather than being a close-in binary.

Dawson, R. I., & Johnson, J. A. 2012, *ApJ*, 756, 122, doi: [10.1088/0004-637X/756/2/122](https://doi.org/10.1088/0004-637X/756/2/122)

—. 2018, *ARA&A*, 56, 175, doi: [10.1146/annurev-astro-081817-051853](https://doi.org/10.1146/annurev-astro-081817-051853)

Dawson, R. I., & Murray-Clay, R. A. 2013, *ApJL*, 767, L24, doi: [10.1088/2041-8205/767/2/L24](https://doi.org/10.1088/2041-8205/767/2/L24)

Díaz, R. F., Damiani, C., Deleuil, M., et al. 2013, *A&A*, 551, L9, doi: [10.1051/0004-6361/201321124](https://doi.org/10.1051/0004-6361/201321124)

Do Ó, C. R., O’Neil, K. K., Konopacky, Q. M., et al. 2023, *AJ*, 166, 48, doi: [10.3847/1538-3881/acdc9a](https://doi.org/10.3847/1538-3881/acdc9a)

Donati, J. F., Kouach, D., Moutou, C., et al. 2020, *MNRAS*, 498, 5684, doi: [10.1093/mnras/staa2569](https://doi.org/10.1093/mnras/staa2569)

Dong, J., Huang, C. X., Dawson, R. I., et al. 2021, *ApJS*, 255, 6, doi: [10.3847/1538-4365/abf73c](https://doi.org/10.3847/1538-4365/abf73c)

- Doyle, L., Cañas, C. I., Libby-Roberts, J. E., et al. 2025, MNRAS, 536, 3745, doi: [10.1093/mnras/stae2819](https://doi.org/10.1093/mnras/stae2819)
- Duquennoy, A., & Mayor, M. 1991, A&A, 248, 485
- Eggleton, P. P., & Kisseleva-Eggleton, L. 2006, Ap&SS, 304, 75, doi: [10.1007/s10509-006-9078-z](https://doi.org/10.1007/s10509-006-9078-z)
- El-Badry, K., Burdge, K. B., van Roestel, J., & Rodriguez, A. C. 2023, The Open Journal of Astrophysics, 6, 33, doi: [10.21105/astro.2307.15729](https://doi.org/10.21105/astro.2307.15729)
- Espinoza, N. 2018, Research Notes of the American Astronomical Society, 2, 209, doi: [10.3847/2515-5172/aaf38](https://doi.org/10.3847/2515-5172/aaf38)
- Espinoza, N., Kossakowski, D., & Brahm, R. 2019, MNRAS, 490, 2262, doi: [10.1093/mnras/stz2688](https://doi.org/10.1093/mnras/stz2688)
- Fabrycky, D., & Tremaine, S. 2007, ApJ, 669, 1298, doi: [10.1086/521702](https://doi.org/10.1086/521702)
- Ferreira dos Santos, T., Rice, M., Wang, X.-Y., & Wang, S. 2024, AJ, 168, 145, doi: [10.3847/1538-3881/ad6b7f](https://doi.org/10.3847/1538-3881/ad6b7f)
- Foreman-Mackey, D. 2016, The Journal of Open Source Software, 1, 24, doi: [10.21105/joss.00024](https://doi.org/10.21105/joss.00024)
- Foreman-Mackey, D., Agol, E., Ambikasaran, S., & Angus, R. 2017, AJ, 154, 220, doi: [10.3847/1538-3881/aa9332](https://doi.org/10.3847/1538-3881/aa9332)
- Fulton, B. J., Petigura, E. A., Blunt, S., & Sinukoff, E. 2018, PASP, 130, 044504, doi: [10.1088/1538-3873/aaa8](https://doi.org/10.1088/1538-3873/aaa8)
- Gaia Collaboration, Brown, A. G. A., Vallenari, A., et al. 2021, A&A, 649, A1, doi: [10.1051/0004-6361/202039657](https://doi.org/10.1051/0004-6361/202039657)
- Gaia Collaboration, Vallenari, A., Brown, A. G. A., et al. 2023, A&A, 674, A1, doi: [10.1051/0004-6361/202243940](https://doi.org/10.1051/0004-6361/202243940)
- Gan, T. 2023, Research Notes of the American Astronomical Society, 7, 226, doi: [10.3847/2515-5172/ad0643](https://doi.org/10.3847/2515-5172/ad0643)
- Gan, T., Cadieux, C., Jahandar, F., et al. 2023, AJ, 166, 165, doi: [10.3847/1538-3881/acf56d](https://doi.org/10.3847/1538-3881/acf56d)
- Giacalone, S., Dai, F., Zanazzi, J. J., et al. 2024, AJ, 168, 189, doi: [10.3847/1538-3881/ad785a](https://doi.org/10.3847/1538-3881/ad785a)
- Goldreich, P., & Sari, R. 2003, ApJ, 585, 1024, doi: [10.1086/346202](https://doi.org/10.1086/346202)
- Goldreich, P., & Soter, S. 1966, Icarus, 5, 375, doi: [10.1016/0019-1035\(66\)90051-0](https://doi.org/10.1016/0019-1035(66)90051-0)
- Grether, D., & Lineweaver, C. H. 2006, ApJ, 640, 1051, doi: [10.1086/500161](https://doi.org/10.1086/500161)
- Halbwachs, J.-L., Pourbaix, D., Arenou, F., et al. 2023, A&A, 674, A9, doi: [10.1051/0004-6361/202243969](https://doi.org/10.1051/0004-6361/202243969)
- Heggie, D. C., & Rasio, F. A. 1996, MNRAS, 282, 1064, doi: [10.1093/mnras/282.3.1064](https://doi.org/10.1093/mnras/282.3.1064)
- Henderson, B. A., Casewell, S. L., Jordán, A., et al. 2024, MNRAS, 533, 2823, doi: [10.1093/mnras/stae1940](https://doi.org/10.1093/mnras/stae1940)
- Hogg, D. W., Myers, A. D., & Bovy, J. 2010, ApJ, 725, 2166, doi: [10.1088/0004-637X/725/2/2166](https://doi.org/10.1088/0004-637X/725/2/2166)
- Holl, B., Sozzetti, A., Sahlmann, J., et al. 2023, A&A, 674, A10, doi: [10.1051/0004-6361/202244161](https://doi.org/10.1051/0004-6361/202244161)
- Howell, S. B., Everett, M. E., Horch, E. P., et al. 2016, ApJL, 829, L2, doi: [10.3847/2041-8205/829/1/L2](https://doi.org/10.3847/2041-8205/829/1/L2)
- Howell, S. B., Everett, M. E., Sherry, W., Horch, E., & Ciardi, D. R. 2011, AJ, 142, 19, doi: [10.1088/0004-6256/142/1/19](https://doi.org/10.1088/0004-6256/142/1/19)
- Huang, C. X., Vanderburg, A., Pál, A., et al. 2020a, Research Notes of the American Astronomical Society, 4, 204, doi: [10.3847/2515-5172/abca2e](https://doi.org/10.3847/2515-5172/abca2e)
- . 2020b, Research Notes of the American Astronomical Society, 4, 206, doi: [10.3847/2515-5172/abca2d](https://doi.org/10.3847/2515-5172/abca2d)
- Husser, T.-O., Wende-von Berg, S., Dreizler, S., et al. 2013, A&A, 553, A6, doi: [10.1051/0004-6361/201219058](https://doi.org/10.1051/0004-6361/201219058)
- Ida, S., Lin, D. N. C., & Nagasawa, M. 2013, ApJ, 775, 42, doi: [10.1088/0004-637X/775/1/42](https://doi.org/10.1088/0004-637X/775/1/42)
- Ida, S., Muto, T., Matsumura, S., & Brasser, R. 2020, MNRAS, 494, 5666, doi: [10.1093/mnras/staa1073](https://doi.org/10.1093/mnras/staa1073)
- Jackson, B., Greenberg, R., & Barnes, R. 2008, ApJ, 678, 1396, doi: [10.1086/529187](https://doi.org/10.1086/529187)
- Jenkins, J. M., Twicken, J. D., McCauliff, S., et al. 2016, in Proc. SPIE, Vol. 9913, Software and Cyberinfrastructure for Astronomy IV, 99133E, doi: [10.1117/12.2233418](https://doi.org/10.1117/12.2233418)
- Kipping, D. M. 2013, MNRAS, 435, 2152, doi: [10.1093/mnras/stt1435](https://doi.org/10.1093/mnras/stt1435)
- Kratte, K., & Lodato, G. 2016, ARA&A, 54, 271, doi: [10.1146/annurev-astro-081915-023307](https://doi.org/10.1146/annurev-astro-081915-023307)
- Kreidberg, L. 2015, PASP, 127, 1161, doi: [10.1086/683602](https://doi.org/10.1086/683602)
- Kunimoto, M., Daylan, T., Guerrero, N., et al. 2022, ApJS, 259, 33, doi: [10.3847/1538-4365/ac5688](https://doi.org/10.3847/1538-4365/ac5688)
- Lai, D., & Muñoz, D. J. 2023, ARA&A, 61, 517, doi: [10.1146/annurev-astro-052622-022933](https://doi.org/10.1146/annurev-astro-052622-022933)
- Larsen, A., Swaby, T. N., Kobulnicky, H. A., et al. 2025, AJ, 169, 246, doi: [10.3847/1538-3881/adbb54](https://doi.org/10.3847/1538-3881/adbb54)
- Laughlin, G., Bodenheimer, P., & Adams, F. C. 1997, ApJ, 482, 420, doi: [10.1086/304125](https://doi.org/10.1086/304125)
- Lightkurve Collaboration, Cardoso, J. V. d. M. a., Hedges, C., et al. 2018, Lightkurve: Kepler and TESS time series analysis in Python. <http://ascl.net/1812.013>
- Lin, D. N. C., Bodenheimer, P., & Richardson, D. C. 1996, Nature, 380, 606, doi: [10.1038/380606a0](https://doi.org/10.1038/380606a0)
- Lin, Z., Gan, T., Wang, S. X., et al. 2023, MNRAS, 523, 6162, doi: [10.1093/mnras/stad1745](https://doi.org/10.1093/mnras/stad1745)
- Ma, B., & Ge, J. 2014, MNRAS, 439, 2781, doi: [10.1093/mnras/stu134](https://doi.org/10.1093/mnras/stu134)
- Mann, A. W., Deacon, N. R., Gaidos, E., et al. 2014, AJ, 147, 160, doi: [10.1088/0004-6256/147/6/160](https://doi.org/10.1088/0004-6256/147/6/160)
- Mann, A. W., Feiden, G. A., Gaidos, E., Boyajian, T., & von Braun, K. 2015, ApJ, 804, 64, doi: [10.1088/0004-637X/804/1/64](https://doi.org/10.1088/0004-637X/804/1/64)
- Mann, A. W., Dupuy, T., Kraus, A. L., et al. 2019, ApJ, 871, 63, doi: [10.3847/1538-4357/aaf3bc](https://doi.org/10.3847/1538-4357/aaf3bc)

- Marcy, G. W., & Butler, R. P. 2000, *PASP*, 112, 137, doi: [10.1086/316516](https://doi.org/10.1086/316516)
- Masci, F. J., Laher, R. R., Rusholme, B., et al. 2019, *PASP*, 131, 018003, doi: [10.1088/1538-3873/aae8ac](https://doi.org/10.1088/1538-3873/aae8ac)
- Nagpal, V., Blunt, S., Bowler, B. P., et al. 2023, *AJ*, 165, 32, doi: [10.3847/1538-3881/ac9fd2](https://doi.org/10.3847/1538-3881/ac9fd2)
- Naoz, S., & Fabrycky, D. C. 2014, *ApJ*, 793, 137, doi: [10.1088/0004-637X/793/2/137](https://doi.org/10.1088/0004-637X/793/2/137)
- Naoz, S., Farr, W. M., Lithwick, Y., Rasio, F. A., & Teyssandier, J. 2011, *Nature*, 473, 187, doi: [10.1038/nature10076](https://doi.org/10.1038/nature10076)
- Newton, E. R., Charbonneau, D., Irwin, J., et al. 2014, *AJ*, 147, 20, doi: [10.1088/0004-6256/147/1/20](https://doi.org/10.1088/0004-6256/147/1/20)
- Pecaut, M. J., & Mamajek, E. E. 2013, *ApJS*, 208, 9, doi: [10.1088/0067-0049/208/1/9](https://doi.org/10.1088/0067-0049/208/1/9)
- Petrovich, C., & Tremaine, S. 2016, *ApJ*, 829, 132, doi: [10.3847/0004-637X/829/2/132](https://doi.org/10.3847/0004-637X/829/2/132)
- Pollack, J. B., Hubickyj, O., Bodenheimer, P., et al. 1996, *Icarus*, 124, 62, doi: [10.1006/icar.1996.0190](https://doi.org/10.1006/icar.1996.0190)
- Psaridi, A., Bouchy, F., Lendl, M., et al. 2022, *A&A*, 664, A94, doi: [10.1051/0004-6361/202243454](https://doi.org/10.1051/0004-6361/202243454)
- Rasio, F. A., & Ford, E. B. 1996, *Science*, 274, 954, doi: [10.1126/science.274.5289.954](https://doi.org/10.1126/science.274.5289.954)
- Ricker, G. R., Winn, J. N., Vanderspek, R., et al. 2015, *Journal of Astronomical Telescopes, Instruments, and Systems*, 1, 014003, doi: [10.1117/1.JATIS.1.1.014003](https://doi.org/10.1117/1.JATIS.1.1.014003)
- Rojas-Ayala, B., Covey, K. R., Muirhead, P. S., & Lloyd, J. P. 2012, *ApJ*, 748, 93, doi: [10.1088/0004-637X/748/2/93](https://doi.org/10.1088/0004-637X/748/2/93)
- Scott, N. J., Howell, S. B., Gnilka, C. L., et al. 2021, *Frontiers in Astronomy and Space Sciences*, 8, 138, doi: [10.3389/fspas.2021.716560](https://doi.org/10.3389/fspas.2021.716560)
- Siverd, R. J., Beatty, T. G., Pepper, J., et al. 2012, *ApJ*, 761, 123, doi: [10.1088/0004-637X/761/2/123](https://doi.org/10.1088/0004-637X/761/2/123)
- Siwek, M., Weinberger, R., & Hernquist, L. 2023, *MNRAS*, 522, 2707, doi: [10.1093/mnras/stad1131](https://doi.org/10.1093/mnras/stad1131)
- Smith, J. C., Stumpe, M. C., Van Cleve, J. E., et al. 2012, *PASP*, 124, 1000, doi: [10.1086/667697](https://doi.org/10.1086/667697)
- Speagle, J. S. 2020, *MNRAS*, 493, 3132, doi: [10.1093/mnras/staa278](https://doi.org/10.1093/mnras/staa278)
- Spiegel, D. S., Burrows, A., & Milsom, J. A. 2011, *ApJ*, 727, 57, doi: [10.1088/0004-637X/727/1/57](https://doi.org/10.1088/0004-637X/727/1/57)
- Stassun, K. G., Collins, K. A., & Gaudi, B. S. 2017, *AJ*, 153, 136, doi: [10.3847/1538-3881/aa5df3](https://doi.org/10.3847/1538-3881/aa5df3)
- Stassun, K. G., & Torres, G. 2016, *AJ*, 152, 180, doi: [10.3847/0004-6256/152/6/180](https://doi.org/10.3847/0004-6256/152/6/180)
- . 2018, *ApJ*, 862, 61, doi: [10.3847/1538-4357/aacafc](https://doi.org/10.3847/1538-4357/aacafc)
- Stassun, K. G., Oelkers, R. J., Paegert, M., et al. 2019, *AJ*, 158, 138, doi: [10.3847/1538-3881/ab3467](https://doi.org/10.3847/1538-3881/ab3467)
- Stefánsson, G., Mahadevan, S., Winn, J. N., et al. 2025, *AJ*, 169, 107, doi: [10.3847/1538-3881/ada9e1](https://doi.org/10.3847/1538-3881/ada9e1)
- Stevenson, A. T., Haswell, C. A., Faria, J. P., et al. 2025, *MNRAS*, 539, 727, doi: [10.1093/mnras/staf502](https://doi.org/10.1093/mnras/staf502)
- Strakhov, I. A., Safonov, B. S., & Cheryasov, D. V. 2023, *Astrophysical Bulletin*, 78, 234, doi: [10.1134/S1990341323020104](https://doi.org/10.1134/S1990341323020104)
- Stumpe, M. C., Smith, J. C., Catanzarite, J. H., et al. 2014, *PASP*, 126, 100, doi: [10.1086/674989](https://doi.org/10.1086/674989)
- Stumpe, M. C., Smith, J. C., Van Cleve, J. E., et al. 2012, *PASP*, 124, 985, doi: [10.1086/667698](https://doi.org/10.1086/667698)
- Terrien, R. C., Mahadevan, S., Bender, C. F., et al. 2012, *ApJL*, 747, L38, doi: [10.1088/2041-8205/747/2/L38](https://doi.org/10.1088/2041-8205/747/2/L38)
- Teyssandier, J., & Lai, D. 2020, *MNRAS*, 495, 3920, doi: [10.1093/mnras/staa1363](https://doi.org/10.1093/mnras/staa1363)
- Tokovinin, A., & Moe, M. 2020, *MNRAS*, 491, 5158, doi: [10.1093/mnras/stz3299](https://doi.org/10.1093/mnras/stz3299)
- Triaud, A. H. M. J., Queloz, D., Bouchy, F., et al. 2009, *A&A*, 506, 377, doi: [10.1051/0004-6361/200911897](https://doi.org/10.1051/0004-6361/200911897)
- Triaud, A. H. M. J., Hebb, L., Anderson, D. R., et al. 2013, *A&A*, 549, A18, doi: [10.1051/0004-6361/201219643](https://doi.org/10.1051/0004-6361/201219643)
- Unger, N., Ségransan, D., Barbato, D., et al. 2023, *A&A*, 680, A16, doi: [10.1051/0004-6361/202347578](https://doi.org/10.1051/0004-6361/202347578)
- Vacca, W. D., Cushing, M. C., & Rayner, J. T. 2003, *PASP*, 115, 389, doi: [10.1086/346193](https://doi.org/10.1086/346193)
- Valli, R., Tiede, C., Vigna-Gómez, A., et al. 2024, *A&A*, 688, A128, doi: [10.1051/0004-6361/202449421](https://doi.org/10.1051/0004-6361/202449421)
- Van Eylen, V., Albrecht, S., Huang, X., et al. 2019, *AJ*, 157, 61, doi: [10.3847/1538-3881/aaf22f](https://doi.org/10.3847/1538-3881/aaf22f)
- Virtanen, P., Gommers, R., Oliphant, T. E., et al. 2020, *Nature Methods*, 17, 261, doi: [10.1038/s41592-019-0686-2](https://doi.org/10.1038/s41592-019-0686-2)
- Vowell, N., Rodriguez, J. E., Latham, D. W., et al. 2025, *arXiv e-prints*, arXiv:2501.09795, doi: [10.48550/arXiv.2501.09795](https://doi.org/10.48550/arXiv.2501.09795)
- Wilson, J. C., Henderson, C. P., Herter, T. L., et al. 2004, in *Proc. SPIE*, Vol. 5492, *Ground-based Instrumentation for Astronomy*, ed. A. F. M. Moorwood & M. Iye, 1295–1305, doi: [10.1117/12.550925](https://doi.org/10.1117/12.550925)
- Wright, E. L., Eisenhardt, P. R. M., Mainzer, A. K., et al. 2010, *AJ*, 140, 1868, doi: [10.1088/0004-6256/140/6/1868](https://doi.org/10.1088/0004-6256/140/6/1868)
- Wu, Y., Hadden, S., Dewberry, J., El-Badry, K., & Matzner, C. D. 2025, *ApJL*, 982, L34, doi: [10.3847/2041-8213/adb751](https://doi.org/10.3847/2041-8213/adb751)
- Zhang, E. Y., Carmichael, T. W., Huber, D., et al. 2025, *arXiv e-prints*, arXiv:2503.05115, doi: [10.48550/arXiv.2503.05115](https://doi.org/10.48550/arXiv.2503.05115)
- Zhou, G., Bakos, G. Á., Bayliss, D., et al. 2019, *AJ*, 157, 31, doi: [10.3847/1538-3881/aaf1bb](https://doi.org/10.3847/1538-3881/aaf1bb)
- Ziegler, C., Tokovinin, A., Briceño, C., et al. 2020, *AJ*, 159, 19, doi: [10.3847/1538-3881/ab55e9](https://doi.org/10.3847/1538-3881/ab55e9)